Numerical investigation on rock fragmentation under decoupled charge blasting

Xudong Li[1], Kewei Liu[1,*], Yanyan Sha[2], Jiacai Yang[1], Ruitao Song[1]

[1] School of Resources and Safety Engineering, Central South University, Changsha, China

[2]Department of Mechanical and Structural Engineering and Materials Science, University of Stavanger, Stavanger, Norway

*Corresponding author. *E-mail address*: kewei_liu@csu.edu.cn

Abstract: Blasting using decoupled charge is extensively applied in rock excavation and rock fragmentation. In this study, the rock fragmentation induced by blasting using decoupled charge is investigated by combined finite element modelling and image-processing. After calibrating the numerical model developed in LS-DYNA against the fragment morphology and fragmentation size distribution (FSD) in three air-coupling blasts and three water-coupling blasts, a series of cubic single-hole models are constructed to simulate rock cracking induced by decoupled charge blasting with various decoupling ratios, distinct coupling mediums and different decoupled charge modes. The simulated fracture networks are obtained by blanking the damaged elements whose damage level is over the threshold of crack formation, and the resulting crack patterns are image-processed using ImageJ to identify fragment size. Then, the blast-created FSDs are characterized by a three-parameter generalized extreme value function, and the FSDs with decoupling ratios, coupling mediums and different decoupled charge modes are quantitatively analyzed and compared. The results show that rock fragmentation becomes finer and the FSD range gets narrower with the decrease in decoupling ratio. Meanwhile, smaller fragment sizes and narrower FSD spans are obtained when changing coupling material from air to water and altering radial decoupling to axial decoupling.

Keywords: Decoupled charge blasting, Rock fragmentation, coupling medium, Numerical simulation.

1 Introduction

Drilling and blasting is the most effective technique for rock excavation and rock fragmentation in mining, and the rock fragmentation caused by blasting is the first stage of the production in mining industry, which plays a significant role in delivering marketable products (An et al., 2017; Li et al., 2022; Tao et al., 2020; Wang et al., 2021a; Yi et al., 2017a, 2017b). In controlled blasting and some production blasting, the borehole is generally decoupled charged, and the rock fracturing in blasting is greatly influenced by decoupled charge mode (radial decoupling charge and axial decoupling charge), decoupling ratio (defined as the borehole diameter over charge diameter K_r in radial decoupling blasting and hole length without stemming over charge length K_a in axial decoupling blasting) and coupling medium. Therefore, it is necessary to investigate the behaviour of rock breakage under blasting using decoupled charge for improving the performance in rock excavation and rock fragmentation with controlled blasting and production blasting.

In conventional blasting, i.e. fully coupled charge blasting, the rock near the borehole is severely pulverized due to violent detonation pressure, and the overall development of rock fracture is extremely unstable because the bifurcation and coalescence of cracks successively occur with fine or small scales, resulting in that the rock disintegration in surrounding rock is often in excess of the requirement (Diehl et al., 2000; Han et al., 2020; Kutter and Fairhurst, 1971). To respond to this situation, decoupled charge blasting is introduced and used in controlled blasting such as presplit blasting and smooth blasting to excavate rock in the desired manner and protect the reserved rock from severe damage (Langefors and Kihlström, 1978). In blasting using decoupled charge, including radially decoupled charge blast and axially decoupled charge blast, the coupling medium between the explosive and the borehole wall is strongly compressed by the high pressure generated by the expansion of detonation products so that the explosion shock/stress waves in coupling medium are rapidly decayed (Chen et al., 2020). When the detonation-induced stress waves arrive at the borehole wall, they transmit and reflect at the interface between the coupling medium and rock several times until the blast-indued stress waves completely attenuate in the coupling medium. Hence, the peak pressure on borehole wall reduces and the duration of blast loading prolongs in decoupled charge blasting compared with those in blasting with fully coupled charge. With these mechanisms, as the gap between explosive and borehole wall becomes thicker, the amount of excessively shattering rock particles in the vicinity of borehole which are generated accompanying the rapidly forming and massively developed short cracks reduce. When the decoupled charge borehole is initiated with a large decoupling ratio, the rock fragmentation is mostly controlled by the propagation and interconnection of long cracks, and a radiation-shape fracture pattern is generated (Pál et al., 2014; Wittel et al., 2004), leading to the formation of large rock blocks. Consequently, the rock fragment size and its distribution range in decoupled charge blasting vary accordingly with the variation in decoupling ratio.

Moreover, the rock fragmentation induced by blasting is also influenced by the coupling medium. The air is the most commonly used coupling material in decoupled charge blasting. When air fills the gap between the explosive and hole-wall, the detonation products quickly expand after explosive initiation and fill the whole borehole because of the high compressibility of air such that a part of the detonation energy is consumed in air compression. Meanwhile, due to the air characteristic of low wave impedance, low transfer efficiency of explosion-induced stress from explosive to air and from air to rock is caused. With these mechanisms, decoupling with air can be employed to reduce extreme rock crushing and is usually applied to alleviate damage and vibration to the reserved rock (Liu et al., 2019; Singh et al., 2014; Tose, 2006). Besides air, water is another frequently used coupling material in decoupled charge blasting, such as perimeter blasting of tunnelling, blasting for building demolition and blasting for permeability improvement in coal seam (Huang and Li, 2015; Yan and Xu, 2005; Yuan et al., 2019). The water is generally characterized by incompressibility and low dissipation of explosion energy. During water-coupling blasting, the water in borehole works as an energy transfer layer and transmits much more energy into the rock mass than air owing to the low energy dissipation of explosion-induced stress waves in water, leading to the creation of smaller rock fragments (Cui et al., 2010; Jang et al., 2018). As a consequence, the fragmentation size distribution generated by decoupled charge blasting is distinctly governed by the filling medium on account of the significantly different mechanical properties of coupling materials.

Many investigations have been conducted on stress field evolution and fracture propagation under blasting using decoupled charge (Dehghani et al., 2020; Li et al., 2020; Liang et al., 2011; Wang et al., 2020; Xia et al., 2018). As early as 1981, the differences in explosion pressure and the fracture evolution between air-coupling blasting and water-coupling blasting were experimentally compared using plexiglass models by Fourney et al. (1981). The piezoelectric pressure transducers were applied to record pressure change during blasting and high-speed photography was used to view the dynamic crack evolution. It was found that there is an increase in both magnitude and duration of explosion pressure in water-coupling blasting compared to air-coupling one (blasting using a water-filled hole with one-fourth the amount of charge produces approximative pressure in rock and longer cracks, and the load duration is about 50% prolonged, compared with blasting using an air-filled hole), which appears to be very effective in initiating and propagating fractures. Using finite element modelling without element erosion or a similar algorithm in AUTODYN code, Zhu et al. (2007, 2008) compared the variations in rock fragmentation induced by blasting coupled with air, sand and water without considering the gas flow into "newly generated fractures", and it was pointed out that compared to the rock blasting with air-filled borehole, it is more efficient in rock breakage when filling the hole with sand or water, and the water coupling intensifies rock fragmentation most. Based on the model experiment, the effects of coupling mediums (air and plasticine) and decoupling coefficients on stress evolution in blasting were investigated with high-speed digital image correlation by Yang et al. (2019). The test results showed that plasticine-coupling increases the peak of explosion-induced stress compared with air-coupling, and with the decoupling ratio increasing, the peak of explosion-induced stress reduces initially fast and then decreases slowly. The same pressure attenuation tendency was reported in the physical tests and numerical simulations (Discrete element method with PFC^{2D}) on water-coupling blasting by Yuan et al. (2019), and they also pointed out that the distribution of the fracture network is strongly correlated to the explosion-induced stress attenuation and there is an optimal decoupling coefficient for the best performance of rock fragmentation. Similarly, the effects of decoupling ratios and coupling materials (air and clay) on the extent of the fractured zone in rock-like material (polymethyl methacrylate) were experimentally studied by Ding et al. (2020) using a digital laser dynamic caustics experimental system. The test results demonstrated that when taking clay as the filling medium, more and longer cracks were formed and the fragmentation was significantly improved. Meanwhile, the dynamic energy release rate of the propagation of blast-induced main cracks increases first and then decreases with the increase of decoupling coefficient. Additionally, the blast-induced fractures inside rock sample and damage characteristics with various decoupling coefficients were experimentally investigated by Zuo et al. (2022) via X-ray computed tomography (CT, the spatial resolution of industrial CT scanning system is 0.5 mm × 0.35 mm × 1 mm) and three-dimensional (3D) rock fracture reconstruction. The experimental results were analyzed from a microscopic perspective that with a small decoupling ratio, the blast-induced crack surface was dominated by intracrystalline fractures while with a smaller charge diameter, the crack surface exhibited transgranular and intergranular coupled fracture modes, accompanying by decreasing rock damage. The above-mentioned studies have partly revealed the mechanisms of the pressure variation and fracture evolution in rock under decoupled charge blasting. However, the effect of decoupled charge including decoupling ratio, coupling medium and decoupled charge mode on the blast-induced fragment size distribution (FSD) is still unclear.

Recently, the blast-induced rock fragmentation with different decoupling ratios and coupling mediums was experimentally investigated by Chi et al. (2022), and the results showed that blasting with a smaller decoupling ratio and the water-decoupled charge generates smaller fragments, while blasting with a larger decoupling ratio and the air-decoupled charge produces bigger fragments. Based on the laboratory tests conducted by Chi et al. (2022), in this study, rock fragmentation under decoupling charge blasting is studied using combined finite element modeling in LS-DYNA (LSTC, 2015) and image-processing using ImageJ (Durda et al., 2015). After reasonably determining the parameters for rock, explosive and coupling materials, the developed numerical model is carefully calibrated against the fragment morphology and FSD of three air-coupling blasts and three water-coupling blasts. Then, based on the verified numerical model, a series of cubic single-hole rock blasting models are built to simulate blast-induced rock fracturing with various decoupling ratios, distinct coupling mediums and different decoupled charge modes. The resulting crack patterns are image-processed to provide quantitative insights into the effects of decoupled charges on blast-induced rock fragmentation. Next, the FSDs obtained by the combined finite element modeling and image-processing are characterized by a three-parameter generalized extreme value function, and the FSDs in decoupled charge blasting with different charge modes, decoupling ratios and coupling mediums are quantitatively analyzed and compared. This study tries to provide novel insights into the formation and variation of rock fragmentation in decoupled charge blasting and supplies some guidance to improve the performances of rock excavation and rock fragmentation in controlled and production blasting.

2. Numerical model and numerical calibration

In the current simulation, finite element modelling with LS-DYNA code is adopted to simulate the rock fragmentation induced by decoupled charge blasting because a variety of constitutive models in LS-DYNA library can properly predict the pressure generated by explosive detonation and the dynamic damage behavior of rock which is extremely important for modelling rock blasting. To ensure the accuracy of numerical modelling, numerical verification is first performed against the results from laboratory-scale tests of three air-coupling blasts and three water-coupling blasts.

2.1. Blasting tests

In blasting tests, 240-mm-diameter and 300-mm-hight cylindrical granite samples were used to investigate the rock fragmentation induced by decoupled charge blasting. The density of rock is 2610 kg/m^3; Poisson's ratio is 0.23, Young's modulus is 43.5 GPa, the average P-wave velocity is 4400 m/s and the static uniaxial compressive strength is 86 MPa (Chi et al., 2022). In each sample, a central borehole with a diameter *D* of 10 mm, 14 mm or 20 mm was axially drilled with a length of 200 mm from the specimen top, and the PENT explosive with a diameter of about 6 mm and a height of about 120 mm was centrally placed at the bottom of borehole. Hence, the decoupling ratios in blasting tests are 5/3, 7/3 and 10/3. Two plastic rings that have an external diameter equal to the blasthole diameter were used as the lining to fix the explosive column in hole centre, as depicted in Fig. 1. The density of PETN is approximately 900 kg/m^3. The gap between PETN and hole-wall was filled with air or water, and the borehole was stemmed with fast-curing cement grout. In blasting, the explosive is ignited at the top of the charge column. After conducting the tests, the fragmentation size distributions induced by decoupled charge blasting were obtained by collecting, weighing and sieving the rock fragments.

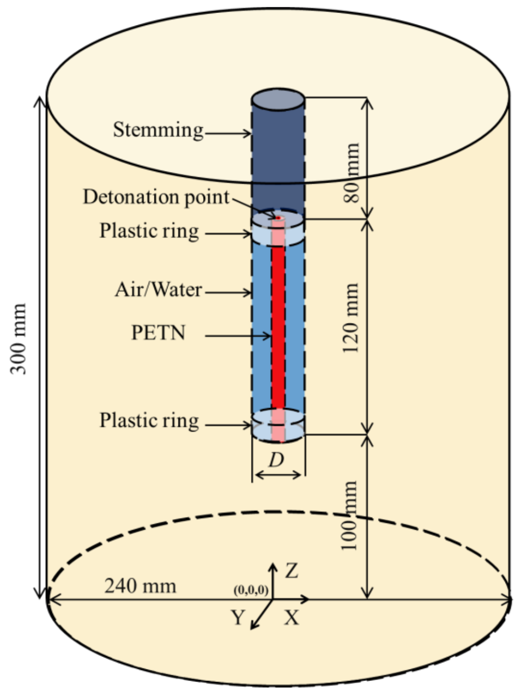

Fig. 1. Sketch of sample in blasting tests

2.2. Numerical model

3D finite element model with the same configuration and size as the test specimen is built, as shown in Fig. 2. The plastic rings that fix the PETN are constructed as air or water due to their low density and strength. The elements at the interfaces between the explosive, air/water, stemming and rock share common nodes, and the *Arbitrary-Lagrange-Euler* (*ALE*) algorithm is applied for explosive and air/water to solve the problems of large deformation in rock blasting while the *Lagrangian* formulation is adopted for stemming and rock. Moreover, the *multi-material ALE* algorithm is employed to control the material mix between explosive and air/water. With these algorithms, the ALE fluids are coupled with the Lagrangian structure, and the robustness of ALE mesh motion and the accuracy of Lagrangian mesh motion within the same framework can avoid problems such as negative volume typically encountered in blasting modelling. In addition, the simulated explosion pressure at the target point (60, 0, 150/mm) is recorded to investigate the pressure variation in the rock under decoupled charge blasting.

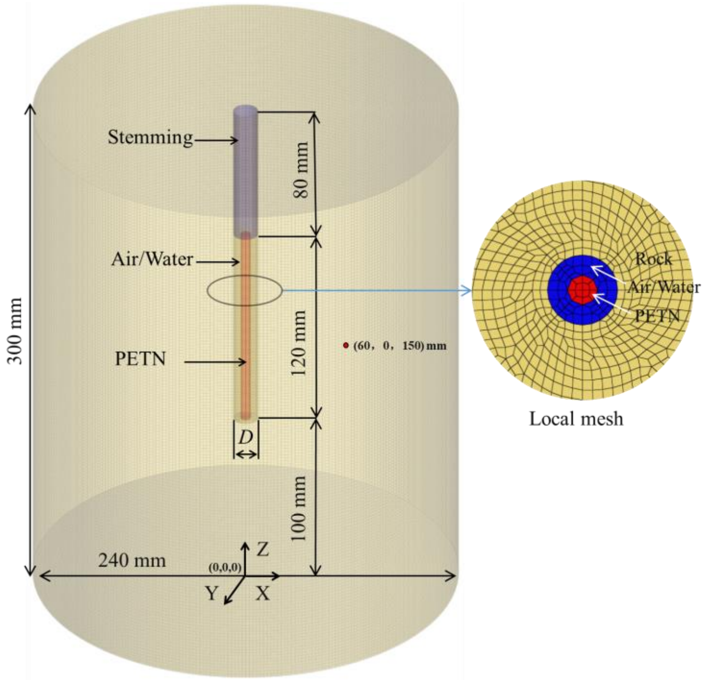

Fig. 2. Finite element model for blasting tests

2.2.1. Material model for rock

Granite is a typical anisotropic material because it consists of a variety of mineral particles and includes pre-existent microcracks, which are not possible to be constructed and simulated numerically because of the limitation of element size in finite element modelling. Hence, in the current numerical modelling, granite is assumed to be an isotropic material, and more symmetrical crack pattern and pressure pattern in granite may be induced due to this assumption of isotropy. There are several constitutive models such as Johnson_Holmquist_II (JH-2) model (Baranowski et al., 2020; Gharehdash et al., 2020; Pu et al., 2021; Wang et al., 2018), Holmquist_Johnson_Cook (HJC) model (Luo et al., 2021; Wang et al., 2021b) and Riedel_Hiermaier_Thoma (RHT) model (Hashemi and Katsabanis, 2021; Huo et al., 2020; Jang et al., 2018; Katsabanis, 2020; Leng et al., 2021; Liu et al., 2018a; Saadatmand Hashemi and Katsabanis, 2020; Zhang et al., 2022) extensively employed to simulate the blast-induced rock response. In the current modelling, the RHT model whose strength criteria are represented in terms of three stress limit surfaces, i.e., the initial elastic yield surface, the failure surface and the residual friction surface is chosen to model rock behavior under decoupled charge blasting because of its advantages of considering the effects of confining pressure, high strain rate, strain hardening and damage softening at the same time (Borrvall and Riedel, 2011). With the use of this model, the behaviors of rock under dynamic loading such as crack initiation, crack propagation and crack branching can be reasonably predicted. During the blasting modelling, the loading scenario for rock element is that the material is elastic before its stress hits the initial elastic yield surface and beyond this surface, it is in a linear strengthening phase in which the rock element deforms plastically before the stress hits the failure surface. When the hardening state reaches the ultimate strength on the failure surface, a parameterized damage model governs the evolution of damage, and the material gradually shifts into the damage-softening phase accompanied by plastic strain accumulation. At last, the material is fully damaged with low residual strength when the stress reaches the residual friction surface. Meanwhile, the pressure in the RHT model is expressed using the Mie–Greisen form with a polynomial Hugoniot curve and a p-α compaction relationship.

In the RHT model, 38 parameters need to be input to LS-DYNA. The basic physical and mechanical parameters such as Density ρ (2610 kg/m^3) and static uniaxial compressive strength f_c (86 MPa) are obtained from laboratory experiments (Chi et al., 2022). The shear modulus G is calculated by $G = E/(2 \times (1 + \gamma))$ in which E is Young's modulus, γ is Poisson's ratio, and G = 17.68 GPa. The uniaxial tensile strength f_t is empirically determined by $f_t = f_c/10$ = 8.6 MPa (Li, 2014). Then, part of the parameters for rock is obtained based on a series of theoretical calculations as follows: the strain rate dependence in the RHT model is described as (Borrvall and Riedel, 2011):

$$F_{\mathrm{r}}(\dot{\varepsilon}_p) = \begin{cases} (\dot{\varepsilon}_p / \dot{\varepsilon}_0^t)^{\beta_t} & (P \le -f_t/3) \\ \dfrac{P + f_{\mathrm{t}}/3}{f_c/3 + f_t/3} (\dot{\varepsilon}_p / \dot{\varepsilon}_0^c)^{\beta_c} - \dfrac{P - f_{\mathrm{c}}/3}{f_{\mathrm{c}}/3 + f_{\mathrm{t}}/3} (\dot{\varepsilon}_p / \dot{\varepsilon}_0^c)^{\beta_t} & (-f_t/3 < P < f_t/3) \\ (\dot{\varepsilon}_p / \dot{\varepsilon}_0^{\mathrm{c}})^{\beta_{\mathrm{c}}} & (P \ge f_c/3) \end{cases} \quad (1)$$

where $F_r(\dot{\varepsilon_p})$ is the strain strength factor, $\dot{\varepsilon_p}$ is the strain rate, P is the pressure, in which $P = (\sigma_1+\sigma_2+\sigma_3)/3$. $\dot{\varepsilon}_0^c$ and $\dot{\varepsilon}_0^t$ are the reference strain rate under compression and tension, respectively, and $\dot{\varepsilon}_0^c = 3.0\times10^{-8}$ s^{-1}, $\dot{\varepsilon}_0^t = 3.0\times10^{-9}$ s^{-1} (LSTC, 2015). β_c and β_t are the material constants for compression and tension, respectively, which are given as (Borrvall and Riedel, 2011):

$$\beta_c = 4/(20+3f_c), \beta_t = 2/(20+f_c) \quad (2)$$

So, β_c and β_t can be calculated as 0.014 and 0.019, respectively.

For a given stress state and rate of loading, the elastic-plastic yield surface in the RHT model is given by (Borrvall and Riedel, 2011):

$$\sigma_y(P^*, \dot{\varepsilon}_p, \varepsilon_p^*) = f_c \sigma_y^*(P^*,\ F_r(\dot{\varepsilon}_p), \varepsilon_p^*) R_3(\theta, P^*) \quad (3)$$

where σ_y^* is the normalized yield function, R_3 denotes the Willam-Warnke function, θ is the lode angle, P^* is the normalized pressure and $P^*=P/f_c$. Moreover, the failure surface is expressed as (Borrvall and Riedel, 2011):

$$\sigma_f^*(P^*, F_r) = \begin{cases} A(P^* - F_r/3 + (A/F_r)^{-1/N})^N & (3P^* \geq F_r) \\ F_r f_s^*/Q_1 + 3P^*(1 - f_s^*/Q_1) & (F_r \geq 3P^* \geq 0) \end{cases} \quad (4)$$

where $Q_1 = R_3(\pi/6,0)$, $\sigma_f^*(F_r)$ is the normalized strength with $\sigma_f^*=\sigma_f / f_c$, in which $\sigma_f = (0.5((\sigma_1 - \sigma_2)^2+(\sigma_2 - \sigma_3)^2+(\sigma_1 - \sigma_3)^2))^{0.5}$. f_s^* and f_t^* are parameters of relative shear strength and relative tensile strength, respectively. $f_t^* = f_t / f_c = 0.10$ and $f_s^* = \tau / f_c$ in which $\tau = A' f_c((\sigma_n - f_t)/f_c)^{B'}$. Pan et al. (2022) gave the values for intact granite, and $A' = 1.32$ and $B' = 0.57$. Thus $f_s^* = 0.32$. A and N are parameters of the failure surface. When rock is under a quasi-static state, i.e. $\dot{\varepsilon_p} = 3.0\times10^{-8}$ s^{-1} and $F_r = 1$, A and N can be calculated through taking the triaxial compressive strengths of rock under various confining pressures obtained by the Hoek-Brown criterion into Eq. (4). For intact granite in the current study, the Hoek-Brown criterion can be written as:

$$\sigma_1 = \sigma_3 + f_c\left(24\frac{\sigma_3}{f_c}+1\right)^{1/2} \tag{5}$$

where σ_1 and σ_3 are the maximum and minimum effective stresses at failure. Next, the mechanical parameters of rock under various confining pressures can be calculated and are listed in Table 1. Taking the values of P^* and σ_f^* under confining stresses of 10 and 100 MPa into Eq. (4), A = 2.50 and N = 0.72 are obtained.

Table 1
Mechanical parameters of rock under various lateral pressures

$\sigma_2 = \sigma_3$/MPa	σ_1/MPa	P/MPa	σ_f/MPa	P^*	σ_f^*
0.00	-8.60	-2.86	8.60	-0.033	0.10
0.00	86.00	28.67	86.00	0.33	1.00
10.00	177.44	65.81	167.44	0.77	1.95
50.00	382.56	160.85	332.56	1.87	3.87
100.00	562.38	254.13	462.38	2.95	5.38
200.00	848.23	416.08	648.23	4.84	7.54

Driven by blast loading, the maximum reduction in strength of RHT model is given as a function of relative pressure (Borrvall and Riedel, 2011):

$$Q(P^*) = Q_0 + BP^* \tag{6}$$

where Q_0 is the ratio between the radii of the tensile and compressive meridians, B is the lode angle dependence factor. Q_0 = 0.68 and B = 0.05 are determined based on the curve regression results reported by Yu (1998). Furthermore, the damage value D in the RHT model is calculated according to (LSTC, 2015):

$$D = \sum(\Delta\varepsilon_p/\varepsilon_f) \tag{7}$$

where $\Delta\varepsilon_p$ is the accumulated plastic strain, ε_f is the failure strain expressed as (LSTC, 2015):

$$\varepsilon_f = D_1 - (P^* - (1 - D)\, P_t^*)^{D2} \tag{8}$$

where P_t^* is the failure cut-off pressure, D_1 and D_2 are damage constants, and D_1 = 0.04 and D_2 = 1.00 are determined from Reference (Brannon and Leelavanichkul, 2009). After running the simulation, D = 0 represents the rock element undamaged whereas D = 1 means that rock element is fully damaged.

Besides, the equation of state (EOS) of the RHT model is described as (Borrvall and Riedel, 2011):

$$P_{EOS} = \frac{1}{\alpha}((B_0 + B_1\mu)\alpha_0\rho_0 e + A_1\mu + A_2\mu^2 + A_3\mu^3) \quad \mu>0 \tag{9}$$

where ρ_0 is the initial density of rock, e is the internal energy per unit mass, μ is the volumetric strain, B_0 and B_1 are constants for polynomial EOS, and $B_0 = B_1 \approx 2s - 1$ in which s is the material constant. α and α_0 are the current and initial porosity, respectively. $B_0 = B_1 = 1.22$, $\alpha_0 = 1.00$ are set according to Reference (Xie et al., 2017). A_1, A_2 and A_3 are the Hugoniot polynomial coefficients which can be calculated by the derived formulation of Xie et al. (2017) as follows:

$$A_1 = \alpha_0\rho_0 c^2 \tag{10a}$$

$$A_2 = \alpha_0\rho_0 c^2(2s-1) \tag{10b}$$

$$A_3 = \alpha_0\rho_0 c^2[(3s-1)(s-1)] \tag{10c}$$

where c is the P-wave velocity in rock. So, A_1 = 50.8 GPa, A_2 = 61.98 GPa and A_3 = 13.02 GPa can be obtained. Besides, the elastic limit pressure, i.e. the pore crush pressure, is taken as 2/3 of the uniaxial compressive strength according to Riedel et al. (2009), which is 57.33 MPa. The remaining parameters are set as defaults (Borrvall and Riedel, 2011), and the parameters used in RHT model for rock are listed in Table 2. In addition, the fast-curing cement grout for stemming is also modelled using the RHT model and the default parameters are used. More details about the RHT model can be found in References (Borrvall and Riedel, 2011; LSTC, 2015; Xie et al., 2017).

Table 2
Parameters for rock

Parameter	Type	Value	Parameter	Type	Value
Mass density ρ (kg/m^3)	*E*	2610	Compressive strain rate dependence exponent β_t	*E*	0.014
Elastic shear modulus G (GPa)	*E*	17.68	Tensile strain rate dependence exponent β_t	*E*	0.019
Eroding plastic strain *EPSF*	*L*	2.0	Volumetric plastic strain fraction in tension *PTF*	*L*	0.001
Parameter for polynomial EOS B_0	*L*	1.22	Compressive yield surface parameter	*L*	0.53

			*GC**		
Parameter for polynomial EOS B_1	*L*	1.22	Tensile yield surface parameter *GT**	*L*	0.70
Parameter for polynomial EOS T_1 (GPa)	*E*	50.80	Shear modulus reduction factor *XI*	*L*	0.50
Parameter for polynomial EOS T_2 (GPa)	*L*	0.0	Damage parameter D_1	*L*	0.04
Failure surface parameter *A*	*E*	2.50	Damage parameter D_2	*L*	1.0
Failure surface parameter *N*	*E*	0.72	Minimum damaged residual strain *EPM*	*L*	0.01
Compressive strength f_c (MPa)	*E*	86	Residual surface parameter *AF*	*L*	1.60
Crush pressure *PEL* (MPa)	*E*	57.33	Residual surface parameter *NF*	*L*	0.61
Relative shear strength f_s*	*E*	0.32	Gruneisen gamma *GAMMA*	*L*	0.0
Relative tensile strength f_t*	*E*	0.10	Hugoniot polynomial coefficient A_1 (GPa)	*E*	50.80
Lode angle dependence factor Q_0	*L*	0.68	Hugoniot polynomial coefficient A_2 (GPa)	*E*	61.98
Lode angle dependence factor *B*	*L*	0.05	Hugoniot polynomial coefficient A_3 (GPa)	*E*	13.02
Reference compressive strain rate *EOC* (S^{-1})	*L*	$3.0E^{-8}$	Compaction pressure *PCO* (GPa)	*L*	6.0
Reference tensile strain rate *ETC* (s^{-1})	*L*	$3.0E^{-9}$	Porosity exponent *NP*	*L*	3.0
Break compressive strain rate *EC* (s^{-1})	*L*	$3.0E^{+22}$	Initial porosity α_0	*L*	1.00
Break tensile strain rate *ET* (s^{-1})	*L*	$3.0E^{+22}$			

Type "*E*" denotes parameters obtained based on experiment; Type "*E*" denotes parameters determined based on literature

2.2.2. Jones-Wilkins-Lee EOS for PETN

The combination of the material type of Mat_High_Explosive_Burn and the EOS of Jones-Wilkins-Lee (JWL) is widely used in LS-DYNA to simulate the pressure generated by the expansion of detonation products (Liu et al., 2018b, 2019; Wei et al., 2009). The JWL EOS precisely defines the detonation pressure *P* as (Lee et al., 1968):

$$P = A\left(1-\frac{\omega}{R_1 V}\right)e^{-R_1 V} + B\left(1-\frac{\omega}{R_2 V}\right)e^{-R_2 V} + \frac{\omega E}{V} \tag{11}$$

where *V* is the volume relative to the undetonated state, *E* is the detonation energy per unit "initial" volume with an initial value of E_0, and *A*, *B*, R_1, R_2 and ω are explosive constants. The detonation velocity (*VOD*) and Chapman-Jouguet pressure (P_{CJ}) of PETN are calculated using the regression equations based on the published data on detonation pressure measurements on PETN (Green and Lee, 2006), and $VOD = (\rho_0 + 0.499)/0.272$ and $P_{CJ} = 18.05\,\rho_0^2 + 17.39\,\rho_0 + 7.45$ (ρ_0 in g/cm^{-3}, *VOD* in km/s and P_{CJ} in GPa). The remaining parameters for explosive are determined with the regression equations reported by Banadaki based on JWL data for PETN at different densities (Banadaki, 2010), and the parameters for PETN are listed in Table 3.

Table 3

Parameters for explosive

ρ_0 (kg/m^3)	*VOD* (km/s)	E_0 (GPa)	P_{CJ}	*A* (GPa)	*B* (GPa)	R_1	R_2	ω
900	5.144	5.00	6.42	441.4	11.60	6.96	1.99	0.24

2.2.3. Linear_Polynomial EOS for air

The material type of Mat_Null together with a specific Linear_Polynomial EOS is extensively employed to model air in LS-DYNA, and this EOS describes the pressure *P* in the air as (LSTC, 2015):

$$P = C_0 + C_1\mu + C_2\mu_2 + C_3\mu_3 + (C_4 + C_5 + C_6\mu_2)E \tag{12}$$

where *E* is the internal energy per volume, μ defines the compression of air by $\mu=(\rho/\rho_0)-1$ with ρ and ρ_0 being the current and initial density of air, respectively. C_0, C_1, C_2, C_3, C_4, C_5 and C_6 are material constants of air, and C_4 and C_5 can be calculated by $C_4 = C_5 = \gamma - 1$ with γ being the ratio of specific heats. The parameters for air are well documented with previous experimental calibrations and are listed in Table 4.

Table 4
Parameters for air

ρ_0 (kg/m^3)	E_0 (J/m^3)	γ	C_0	C_1	C_2	C_3	C_4	C_5	C_6
1.29	2.5×10^5	1.4	0	0	0	0	0.4	0.4	0

2.2.4. Gruneisen EOS for water

The water is modeled by the material type of Mat_Null combined with the Gruneisen EOS, and this EOS defines pressure *P* for compressed water as (LSTC, 2015):

$$P = \frac{\rho_0 C^2 \mu \left[1 + \left(1 - \frac{\gamma_0}{2}\right)\mu - \frac{\alpha}{2}\mu^2\right]}{\left[1 - (S_1 - 1)\mu - S_2\frac{\mu^2}{\mu+1} - S_3\frac{\mu^3}{(\mu+1)^2}\right]^2} + (\gamma_0 + \alpha\mu)E \tag{13}$$

where γ_0 is the Gruneisen gamma, α is the first order volume correction to γ_0, μ is defined as ρ/ρ_0-1 with ρ and ρ_0 being the current and initial density of water, respectively. *C* is the intercept of v_s-v_p curve, *E* is the internal energy per unit "initial" volume with an initial value of E_0, and S_1, S_2 and S_3 are the coefficients of the slope of the v_s-v_p curve. This combination in LS-DYNA is widely used for simulating water-filled blasting and underwater explosion (Zhang et al., 2012;

Zhang et al., 2014), and the parameters of water are also well documented with previous experimental verifications. Thus, the calibrated parameters in previous study for water are employed in the current simulation and no parametric study on the compressibility of water for the water-coupling blasts is conducted. This may lead to a little difference in stress transfer from explosive transmitting water to rock between simulation and real blasting. However, compared to the extremely high pressure in blasting, this tiny difference can be neglected. The parameters for water are listed in Table 5.

Table 5
Parameters for water

ρ_0 (kg/m^3)	C (m/s)	E_0 (J/m^3)	S_1	S_2	S_3	γ_0	α	V_0
1000	1480	1.89×10^6	2.56	-1.986	1.2268	0.35	0	1.0

2.3. Numerical calibration

The results of rock fragmentation in tests of decoupled charge blasting are presented in Fig. 3. As can be seen, after running the physical tests, the sample S1 (air-coupling, hole diameter of 20 mm, K_r = 3.33) was mainly fragmented into several large blocks, and each of large fragment is almost a quarter cylinder; sample S2 (air-coupling, hole diameter of 14 mm, K_r = 2.33) was primarily disintegrated into eight fragments being almost half of a quarter cylinder and several smaller fragments; sample S3 (air-coupling, hole diameter of 10 mm, K_r = 1.67) was broken into many small fragments. The samples S4, S5 and S6 have borehole diameters of 20 mm, 14 mm and 10 mm and decoupling ratios K_r of 3.33, 2.33 and 1.67 in the sequence and were water-filled. Similar to air-coupling blasting, the fragment sizes of samples S4–S6 show a decreasing tendency with the decrease of hole diameter, without fragments larger than 180 mm. In comparison, the variation in rock fragmentation under water-coupling blasting of samples S4-S6 is not obvious as that under air-coupling blasting of samples S1-S3.

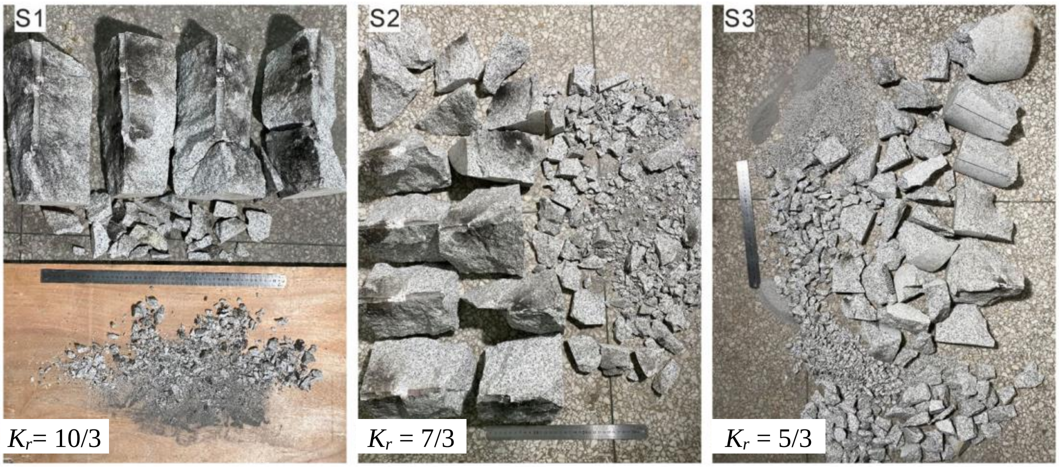

Air-coupling blasting

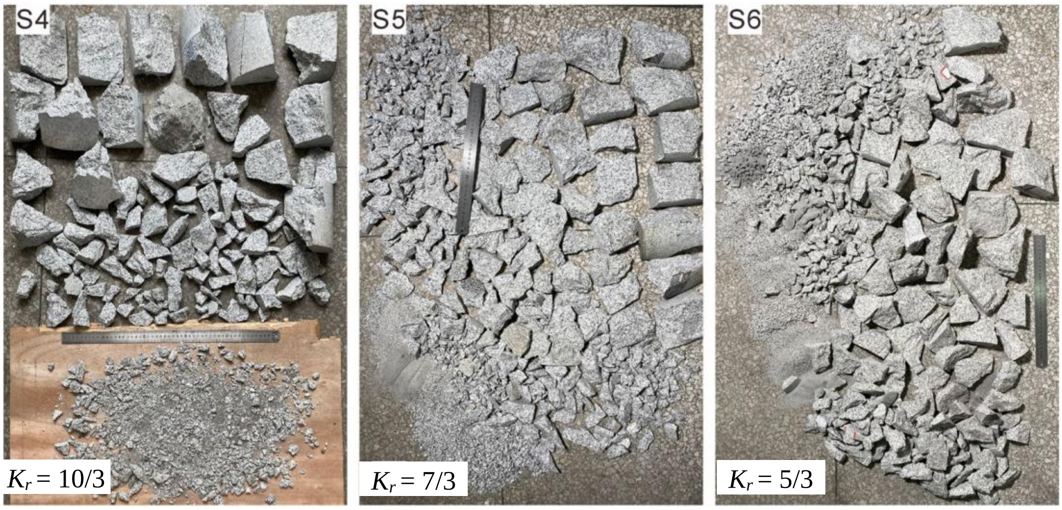

Water-coupling blasting

Fig. 3 rock fragmentation after blast testing

These results of rock breakage in specimens of S1-S3 under air-coupling blasting and specimens of S4-S6 under water-coupling blasting are simulated using the developed numerical model with the above-introduced material models and EOSs in LS-DYNA. Before the modelling of the blasting tests, mesh size convergence test is conducted with different element sizes, and the simulation results of air-coupling blasting for Sample S2 are presented as examples in Fig. 4. The numerical results in the mesh size convergence test show that the damage patterns are almost the same while smaller mesh size gives more small cracks and takes much longer computational time. In the mesh size convergence test, the explicit time integration scheme with one-point quadrature, which is a typical integration scheme of hexahedral element in LS-DYNA for saving computing memory and reducing computational time, is invoked and the time step Δt is shorter than the time that blast stress wave propagates crossing the minimum side length of any element $l_{\min}$, i.e.

$$\Delta t < l_{\min}/C \tag{14}$$

where C is the propagation velocity of the explosion-induced stress wave. Besides, the value of minimum Δt /average Δt is larger than 0.95 when the mesh size is larger than 2 mm×2 mm ×2 mm, indicating that the numerical model developed in the current study runs stably and is reasonable. Finally, to balance the simulation reliability and computational time, the mesh size of 2 mm×2 mm ×2 mm is adopted, and this model is discretized with 1 744 200 hexahedral elements.

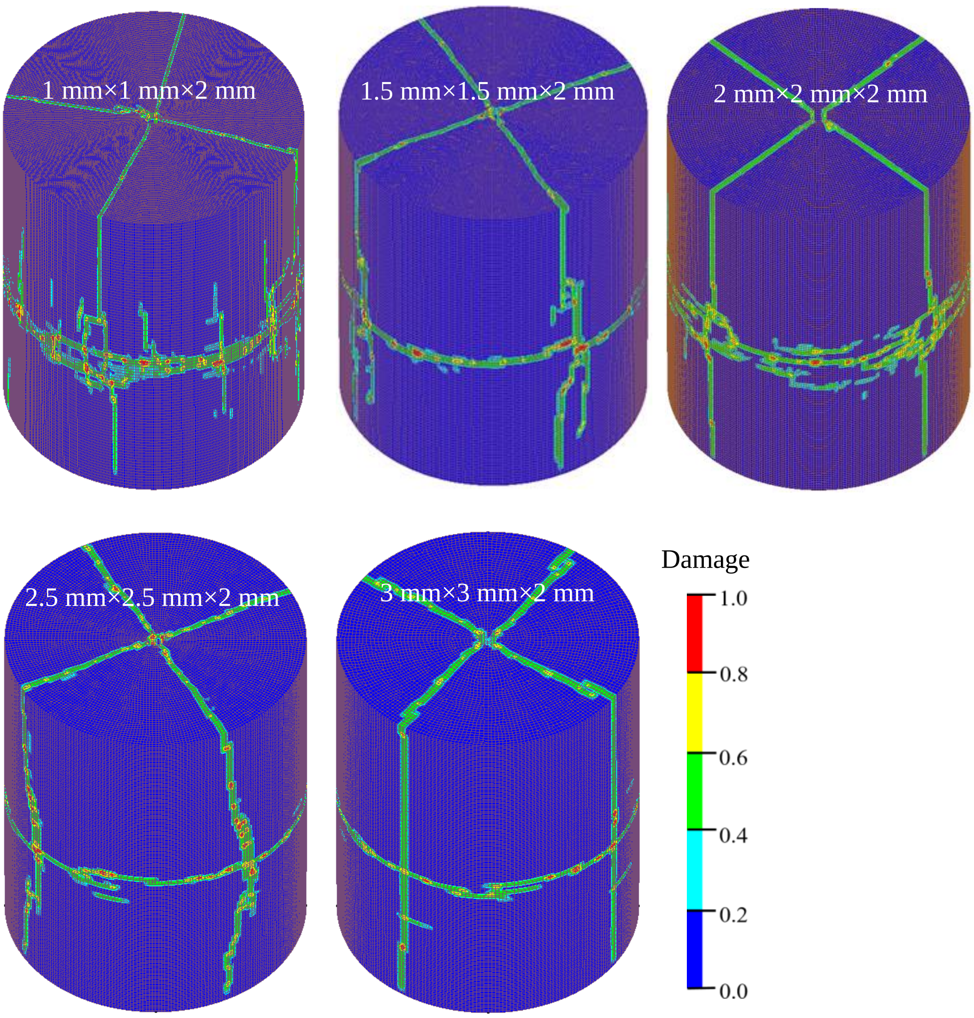

Fig. 4 Damage patterns under air-coupling blasting (S2) with various mesh sizes

Using the mesh size of 2 mm×2 mm×2 mm, three air-coupling blasts and three water-coupling blasts are simulated, and the corresponding damage evolution processes and time-history curves of explosion-induced pressure at target point are presented in Figs. 5(a) and 5(b), respectively. In the current numerical modelling, the overall crack pattern is homogeneous in the radial direction of the model, but some heterogeneous small cracks are generated due to the use of RHT model. With the using of this model, the behaviours of rock under dynamic loading such as crack initiation, crack propagation and crack branching can be reasonably predicted so that the phenomenon of heterogeneous rock fracturing which is generally observed in actual blast is also modelled.

After detonation, a damage zone near the detonation point is immediately created due to high detonation pressure created by the burning of explosive column ($t = 2.5\times10^{-5}$ s). Then, the blast-induced cracks extend downward and outward. At this stage, the rock sample is gradually fragmented with the development of radial cracks and tensile damage in the vicinity of sample surface, which is mainly induced by the tensile component and the reflection of explosion-induced stress waves ($2.5\times10^{-5}\ \text{s} \leq t \leq 7\times10^{-5}\ \text{s}$). After that, the blast-created fractures propagate upward until reaching the top surface of sample, which is also resulted by the tensile stress and reflected stress waves. As can be seen in Fig. 5(a), with the same charge diameter, more extensive cracks are formed under blasting with smaller borehole size, while more blast-indued fractures are generated after the detonation of decoupled charged borehole using water-coupling. This is because a narrower gap between charge and borehole wall and water-coupling produces a higher explosion pressure in rock, as can be observed in Fig. 5(b). In the current numerical modelling, the calculation is terminated when no new crack forms and crack extension arrests, and the computational duration is 3×10^{-4} ms.

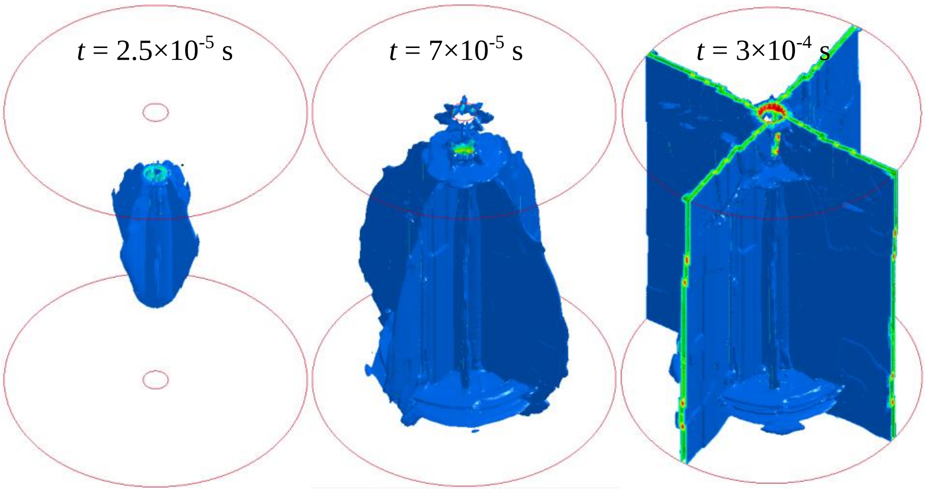
t = 2.5×10-5 s
t = 7×10-5 s
t = 3×10-4 s

S1

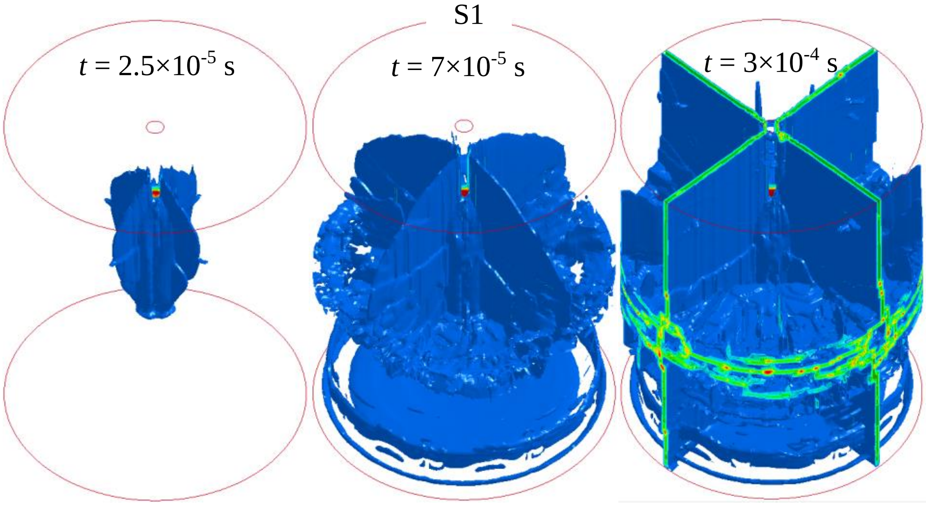
t = 2.5×10-5 s
t = 7×10-5 s
t = 3×10-4 s

S2

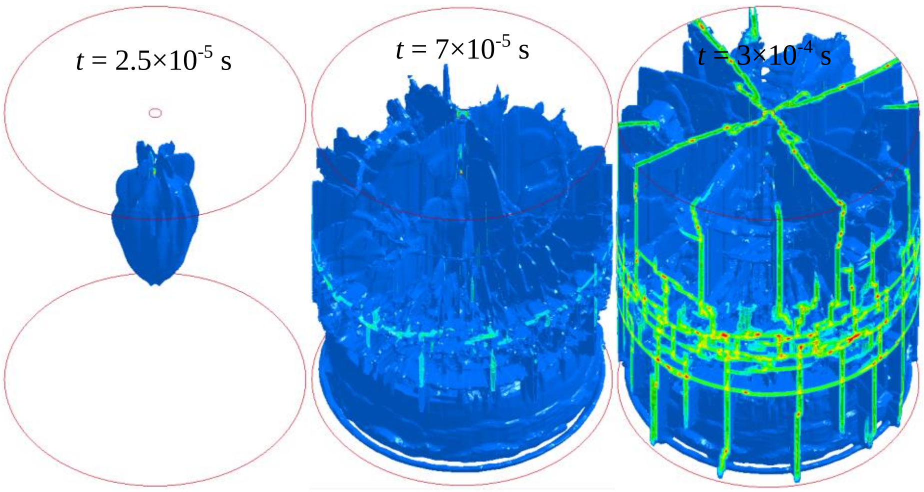
t = 2.5×10-5 s
t = 7×10-5 s
t = 3×10-4 s

S3

(a)

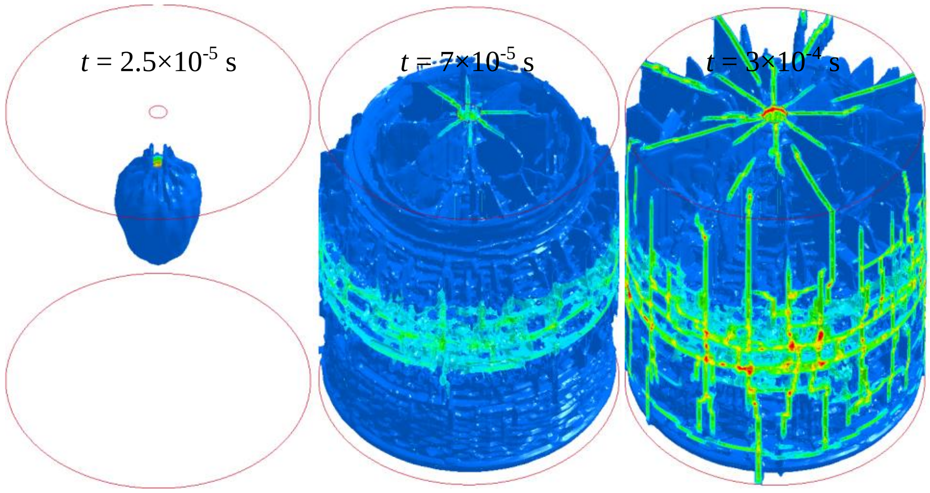

t = 2.5×10^-5 s
t = 7×10^-5 s
t = 3×10^-4 s

S4

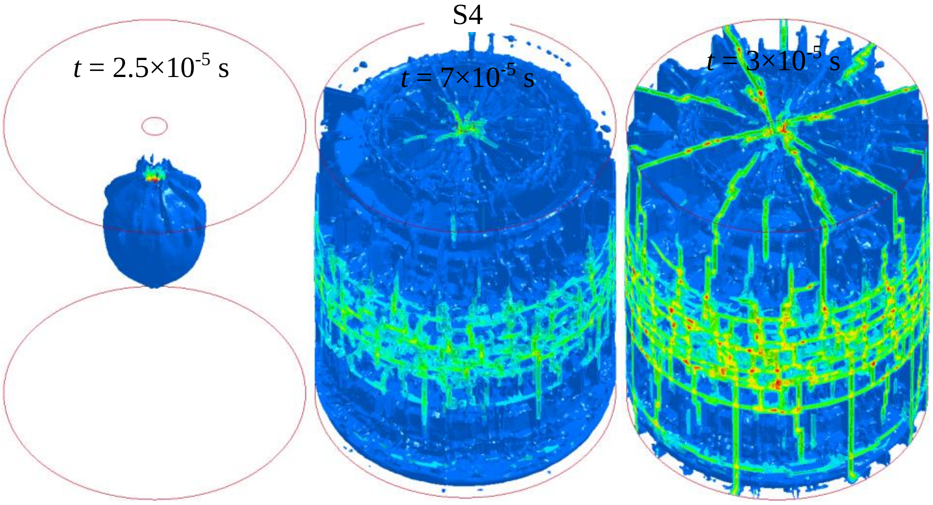

t = 2.5×10^-5 s
t = 7×10^-5 s
t = 3×10^-5 s

S5

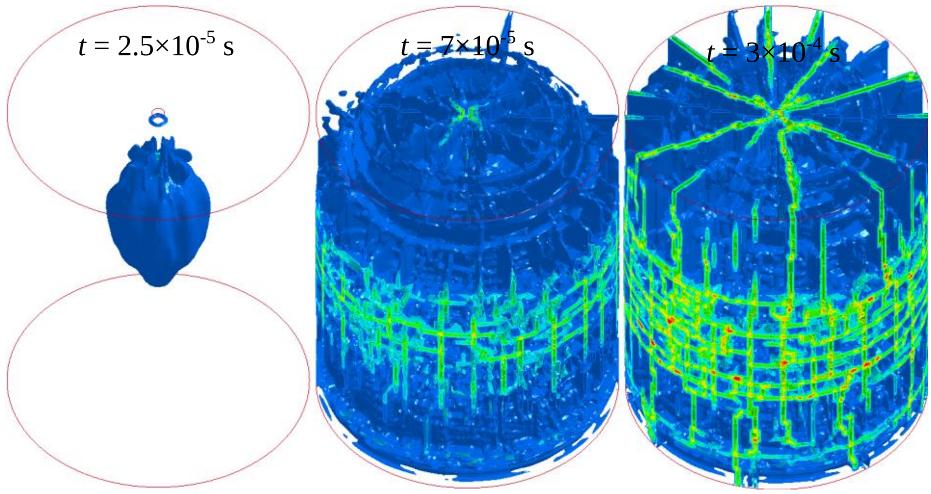

t = 2.5×10^-5 s
t = 7×10^-5 s
t = 3×10^-4 s

S6

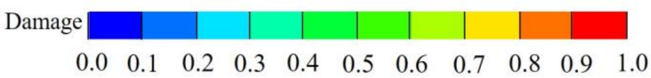

Damage
0.0 0.1 0.2 0.3 0.4 0.5 0.6 0.7 0.8 0.9 1.0

(b)

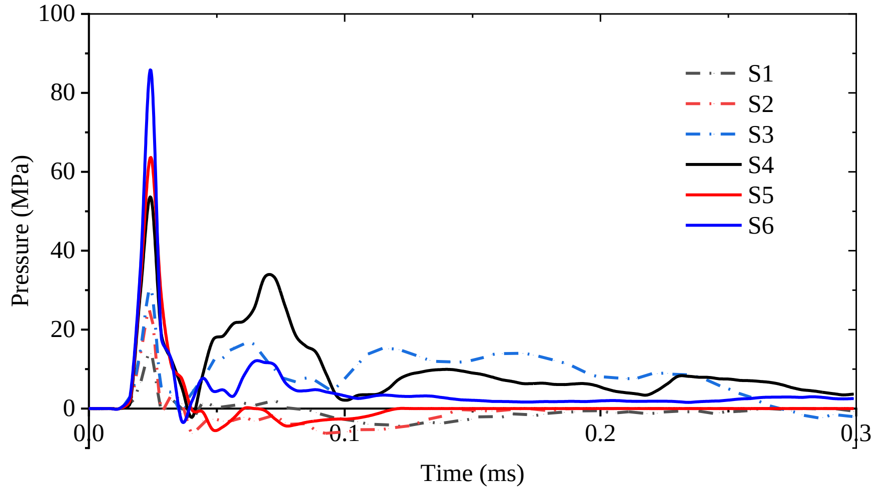

Fig. 5 Simulation of blast tests: (a) Damage pattern evolution, (b) History curves of explosion-induced pressure at the target point

The simulated damage patterns for the abovementioned blast tests are shown in Fig. 6(a). It should be pointed out that in the current study, no element erosion algorithm is used during calculation since the element deletion is non-conservative energetically and may distort the transmission of explosion-induced stress waves, resulting in unrealistic rock cracking (Bobaru and·Zhang, 2016, Song et al. 2008). In the current study, an alternative method in post-processing using the Pre-post code is employed to evaluate rock fracture and rock disintegration. During blasting simulation, the damage of rock material (*D*) accumulates from 0 to 1, and the *D* denotes the damage extent of rock element from slight degradation to complete failure. Under this situation, the critical damage for rock cracking can be determined though comparing the simulated crack pattern after blanking the damaged rock element with a certain level (an example of simulated crack patterns with different damage levels of S2 is presented in Fig. 6(b) with red background color), and the tested fragment morphology, as shown in Fig. 3. After comprising, it is apparent that small damage level (≤ 0.3) for blanking element produces too large cracks whereas large damage level (≥ 0.5) gives too few cracks, which is unreasonable for generating simulated rock cracks. So, a critical value of D = 0.4 is obtained for the generation of rock fracture. Then, the simulated crack patterns for all blast tests can be obtained by blanking rock elements whose damage level is over 0.4 in the Pre-post, and the resulting fracture networks for 6 blast tests are given in Fig. 6(c).

(a)

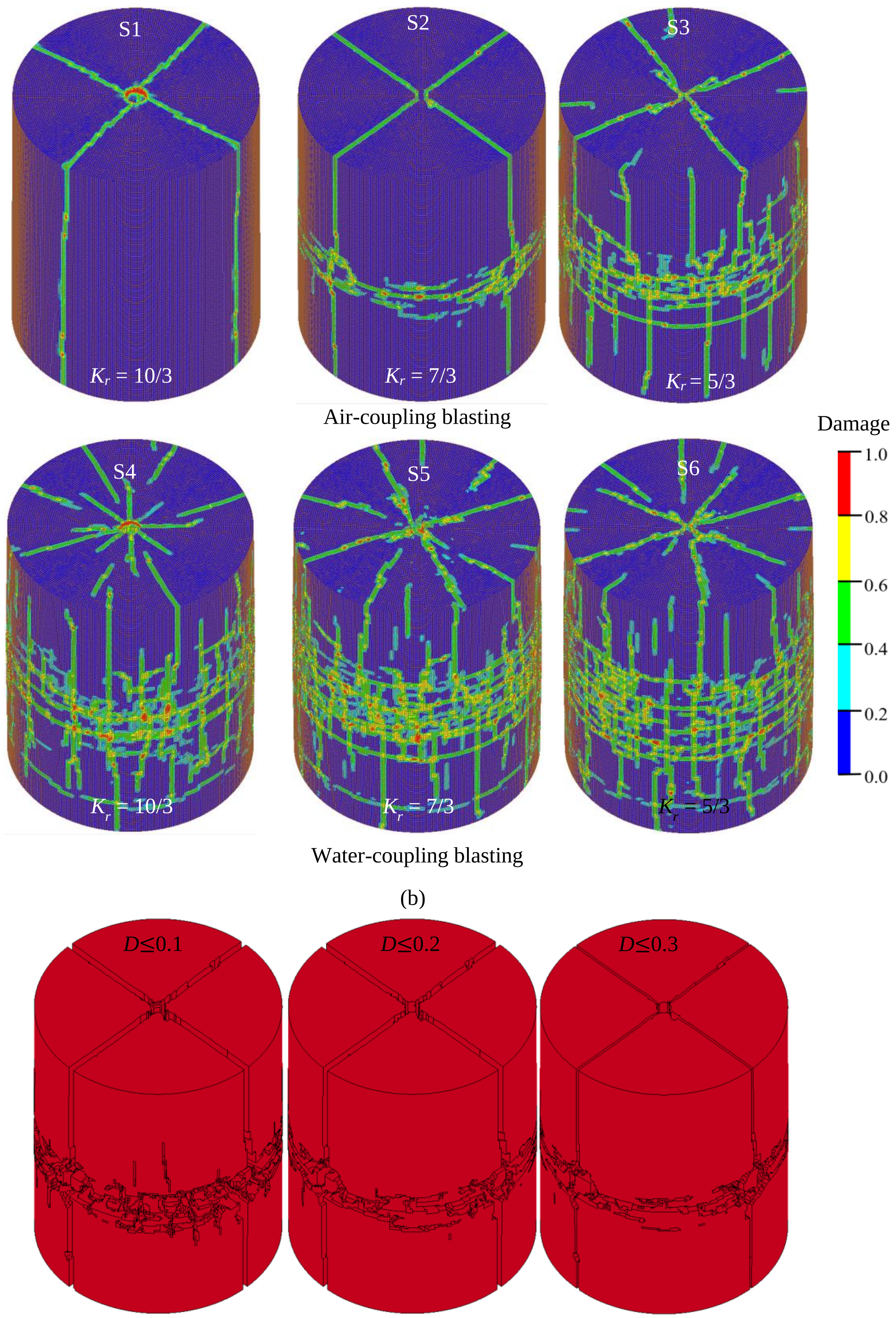

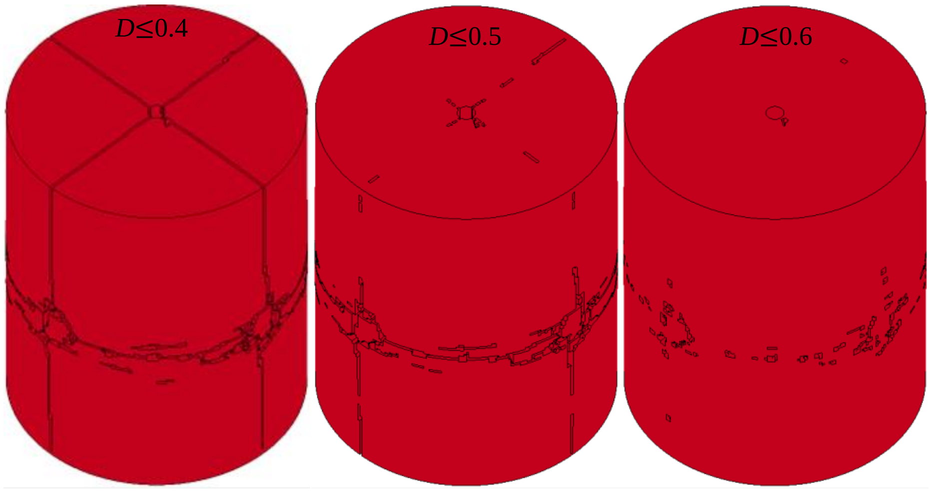

(c)

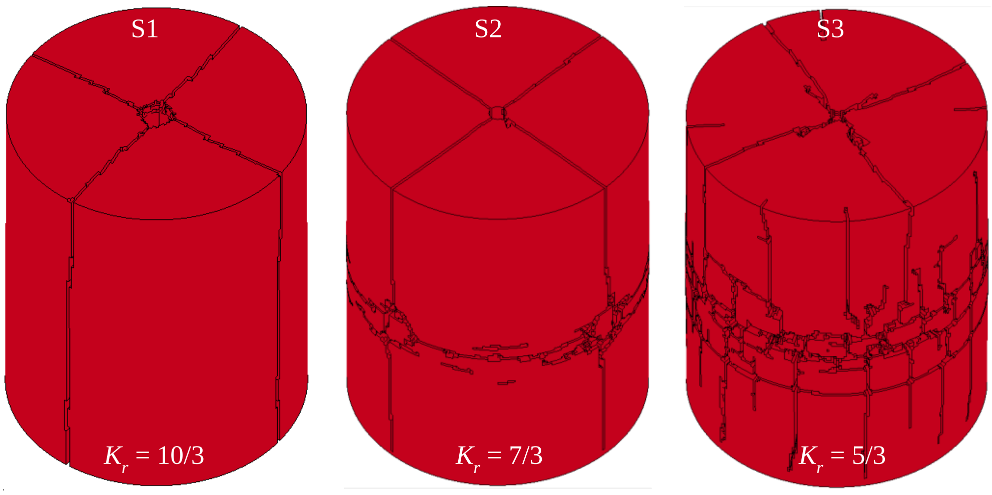

Air-coupling blasting

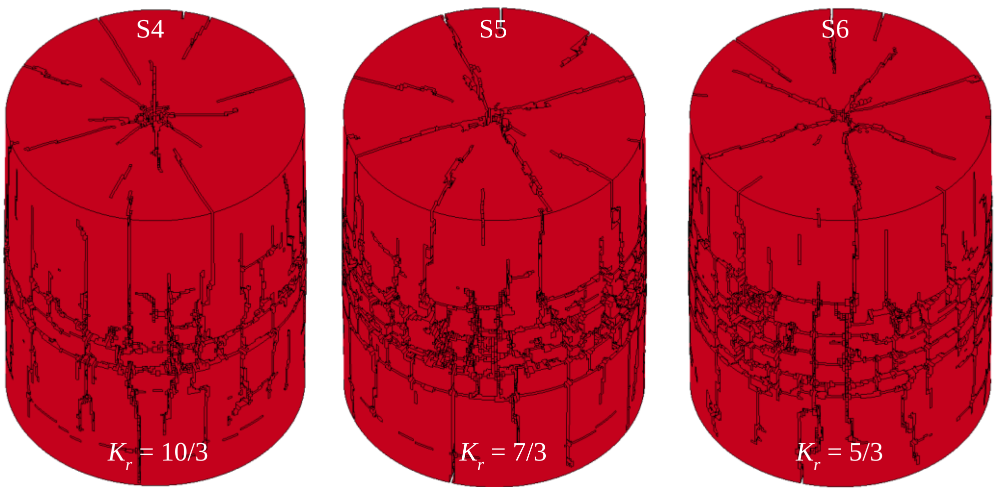

Water-coupling blasting

Fig. 6 Simulation results of rock blast tests (a) the final damage crack patterns, (b) crack patterns with different damage levels of test S2 and (c) fracture networks after blanking damaged rock elements ($D \leq 0.4$)

As can be seen in Fig. 6(c), the simulated cracks in sample S1 run through the whole specimen and break it into 4 fragments (quarter cylinder), and sample S2 is fragmented into 8 main large pieces (about half of a quarter cylinder). Sample S3 is broken into smaller fragments due to the narrow air gap. By contrast, samples S4-S6 are disintegrated into more and smaller pieces than samples S1-S3 because water-coupling transmits higher explosion-induced stress to rock. Similar to the physical tests, the simulations of water-coupling blasting give rock fractures with not much difference. By comparing the fragment morphology in blasting tests and rock fracturing in numerical simulations, it can be pointed out that the rock fracture patterns obtained in simulations agree well with the cracking modes in physical experiments.

Noting that no rock fragment detaches and drops from granite sample in simulation because of finite element modelling. To add reliability to the current simulation, the FSDs are obtained by image-processing the simulated crack patterns and compared with those from blasting tests. After blanking the rock element damage level exceeding 0.4, the numerical model is uniformly cut at $x = 0$ mm, $y = 0$ mm, and $z = 75$, 150 and 225 mm, and the geometry information of fragmentation in these 5 cut surfaces is identified using the image-processing code ImageJ (Durda et al., 2015). The resulting distributions of fragment size in these 5 cut surfaces are merged to represent the overall fragmentation in simulation. The comparison of cumulative frequency distributions of fragment size obtained by combined numerical modelling and image-processing, and from physical testing is shown in Fig. 7. As can be seen, the size and the distribution span of fragment increase with the increase of decoupling ratio. Meanwhile, in both air-coupling blasting and water-coupling blasting, the simulated FSDs are well consistent with those in the blasting experiment. Based on the good agreements in rock breakage and FSD between blasting test and numerical simulation, it can be concluded that the developed numerical model is suitable and applicable for modelling rock fragmentation induced by decoupled charge blasting using air-coupling and water-coupling with free surfaces.

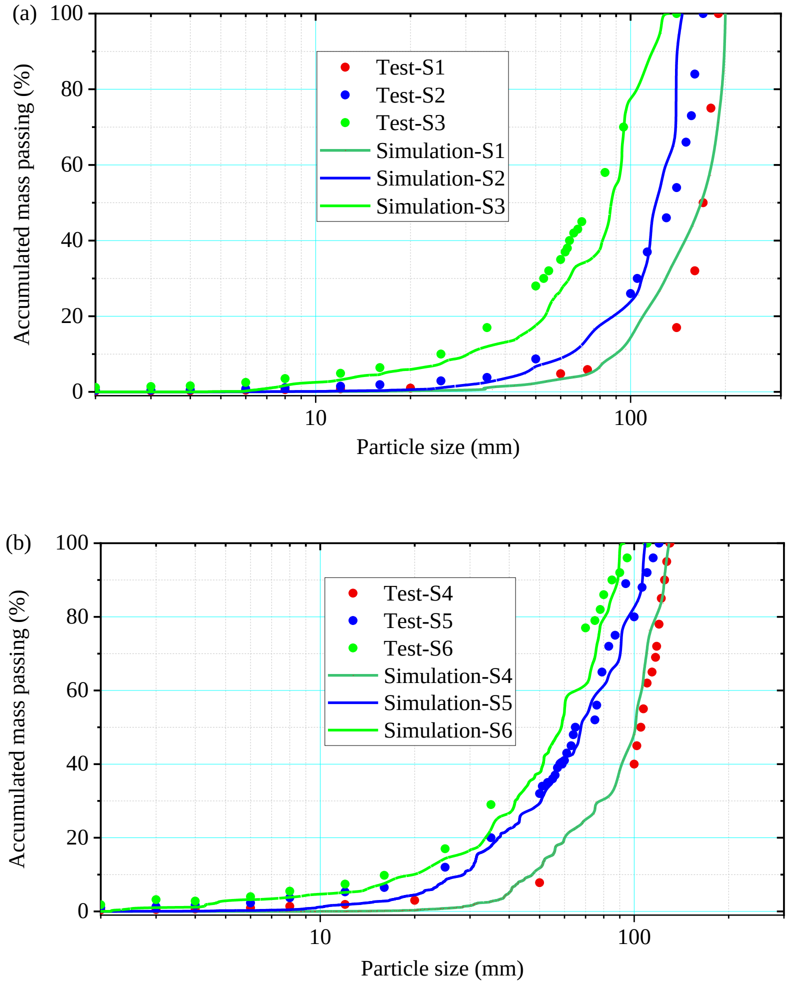

Fig. 7 Comparison of tested and simulated FSDs: (a) FSDs in air-coupling blasting, (b) FSDs in water-coupling blasting

3. Numerical modelling of rock fragmentation in decoupled charge blasting

3.1. Computational model

In this section, the cubic single-borehole models with a hole diameter *D* of 42 mm which is commonly used in controlled blasting in China are built to investigate the rock fragmentation induced by decoupled charge blasting, as shown in Fig. 8. Considering the specific charge commonly used in practical blasting, the side length of model is set as 1 m, and the stemming length at model top and bottom is 0.1 m. Two decoupled charge modes, i.e. radially decoupled charge and axially decoupled charge, two coupling mediums, i.e. air and water, and seven decoupling ratios (4/3, 5/3, 6/3, 7/3, 8/3, 9/3 and 10/3) are considered in the present simulation.

Different from the blasting tests introduced in Section 2, the decoupling ratio in the computational model is controlled by changing charge diameter or charge length instead of borehole diameter. The explosive is detonated at the centre of the model, i.e., at the middle point of charge column (z = 0.5 m). All boundaries of model are set as free boundaries because free boundaries generally exist in actual blasting such as smoothwall blasting. Mesh size convergence tests are carried out with different meshes to minimize the effect of mesh size on numerical results, and the crack pattern is the main issue checked because of the topic of rock fragmentation. After the mesh size convergence test, the model is finally discretized with 1 014 400 hexahedral elements. The elements with a size of 1 mm × 1 mm × 10 mm mesh for explosive, and the elements with a size of 10 mm × 10 mm × 10 mm mesh for rock. It should be pointed out that the mesh size varies in the vicinity of the hole and the max/min length for explosive element is 10 whereas it is 2 for rock element. The common nodes are shared in the elements at the interfaces between the explosive, air/water, rock and stemming, and the large deformation and material mix near the decoupling charge are solved by the *multi-material ALE* algorithm. An MPP LS-DYNA solver (version 8.0) with 28 Cores is used to run this modelling, and half an hour is taken for the typical simulation of this class of model. During calculation, the explosion pressure at the target point (0.25, 0, 0.5/m) is recorded to investigate the pressure attenuation in rock under decoupled charge blasting.

After running the following calculations and generating fracture networks, 9 cut surfaces (x = − 0.25, 0, and 0.25 m; y = − 0.25, 0 m and 0.25 m; z = 0.25, 0.5, and 0.75 m) are chosen to cut this model uniformly and are image-processed. The resulting FSDs of these 9 cut surfaces are emerged to represent the overall fragmentation created by decoupled charge blasting. Then, a three-parameter generalized extreme value (GEV) function (Hogan et al., 2012; Hou et al., 2015; Shen et al., 2017), which performs well in characterizing the FSD of rock under dynamic loading (Hogan et al. 2012), is applied to fit the data of fragment size, and this function is expressed as:

$$F(d;\mu,\sigma,\xi)=\exp\left\{-\left[1+\xi\left(\frac{d-\mu}{\sigma}\right)\right]^{-1/\xi}\right\} \tag{15}$$

where μ is the location parameter related to the average fragment size, σ is the scale parameter that controls the range of the FSD, and ξ is the shape parameter.

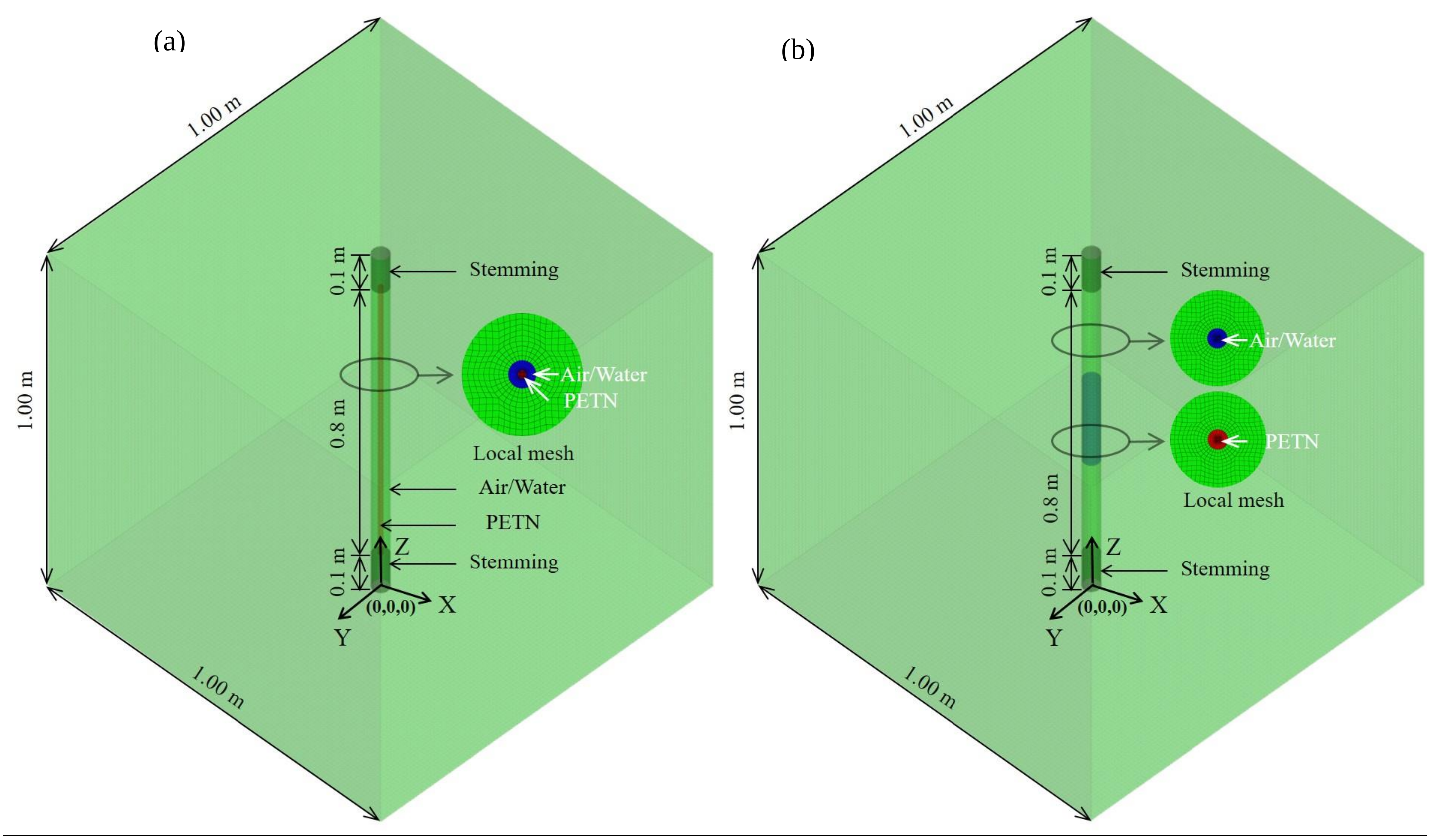

Fig. 8 Configuration and local mesh of the computational models: (a) radially decoupled charge model, (b) axially decoupled charge model

3.2. Rock fragmentation induced by radially decoupled charge blasting

Based on the calibrated material models and EOSs, the rock fragmentation induced by radially decoupled charge blasting with coupling materials of air and water, and different coupling ratios is first simulated, and the evolutions of explosion pressure and damage pattern in blasting are demonstrated using transparent view in Fig. 9. Besides, the time-history curves of explosion pressure at target point are presented in Fig. 10.

It can be found that after the initiation of the radially decoupling charge borehole, the explosion-induced pressure radially radiates away from borehole. Immediately, a crushed zone is generated in the vicinity of borehole due to the high explosion pressure, and the size of this crushed zone increases with the increase of charge diameter while it is larger in water-coupling blasting than air-coupling one. Then, the radial cracks extend in the rock because the tensile stress component of explosion-induced stress waves exceeds the tensile strength of rock, and they finally reach the free surface of rock and disintegrate rock into fragments. During this process, the spalling damage is generated near the surface due to the reflection of explosion-induced stress waves and it intensifies greatly with the decrease of decoupling ratio. Consequently, the radial cracks interact with spalling cracks, forming the final crack patterns. As expected, a larger high-pressure zone, as presented in Fig. 9, and higher pressure, as shown in Fig. 10, are formed by the detonation of decoupled charge with large charge diameter and water-coupling due to more explosive and great stress transmission performance of water, and therefore more damage cracks are formed with smaller decoupling ratio and water-coupling.

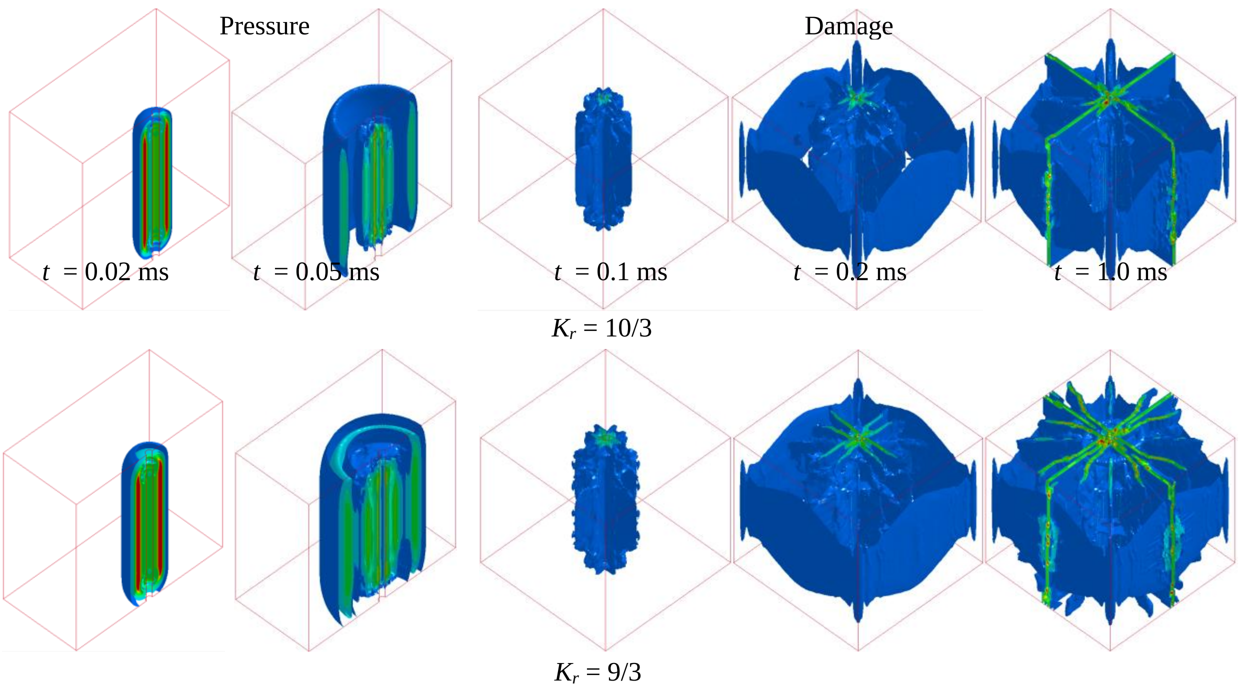

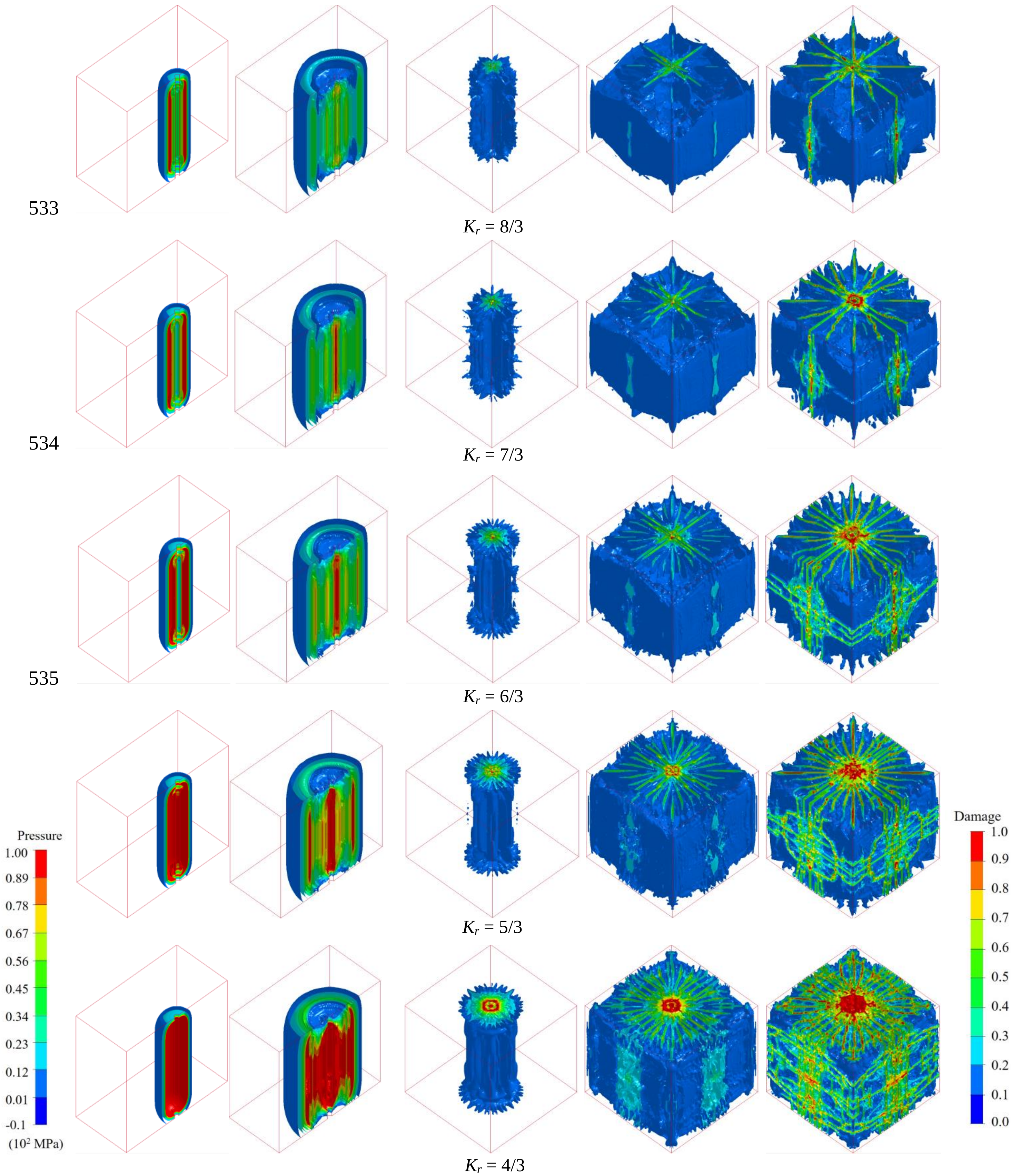

K_r = 8/3
K_r = 7/3
K_r = 6/3
K_r = 5/3
K_r = 4/3
Pressure
1.00
0.89
0.78
0.67
0.56
0.45
0.34
0.23
0.12
0.01
-0.1
(10^2 MPa)
Damage
1.0
0.9
0.8
0.7
0.6
0.5
0.4
0.3
0.2
0.1
0.0

(a)

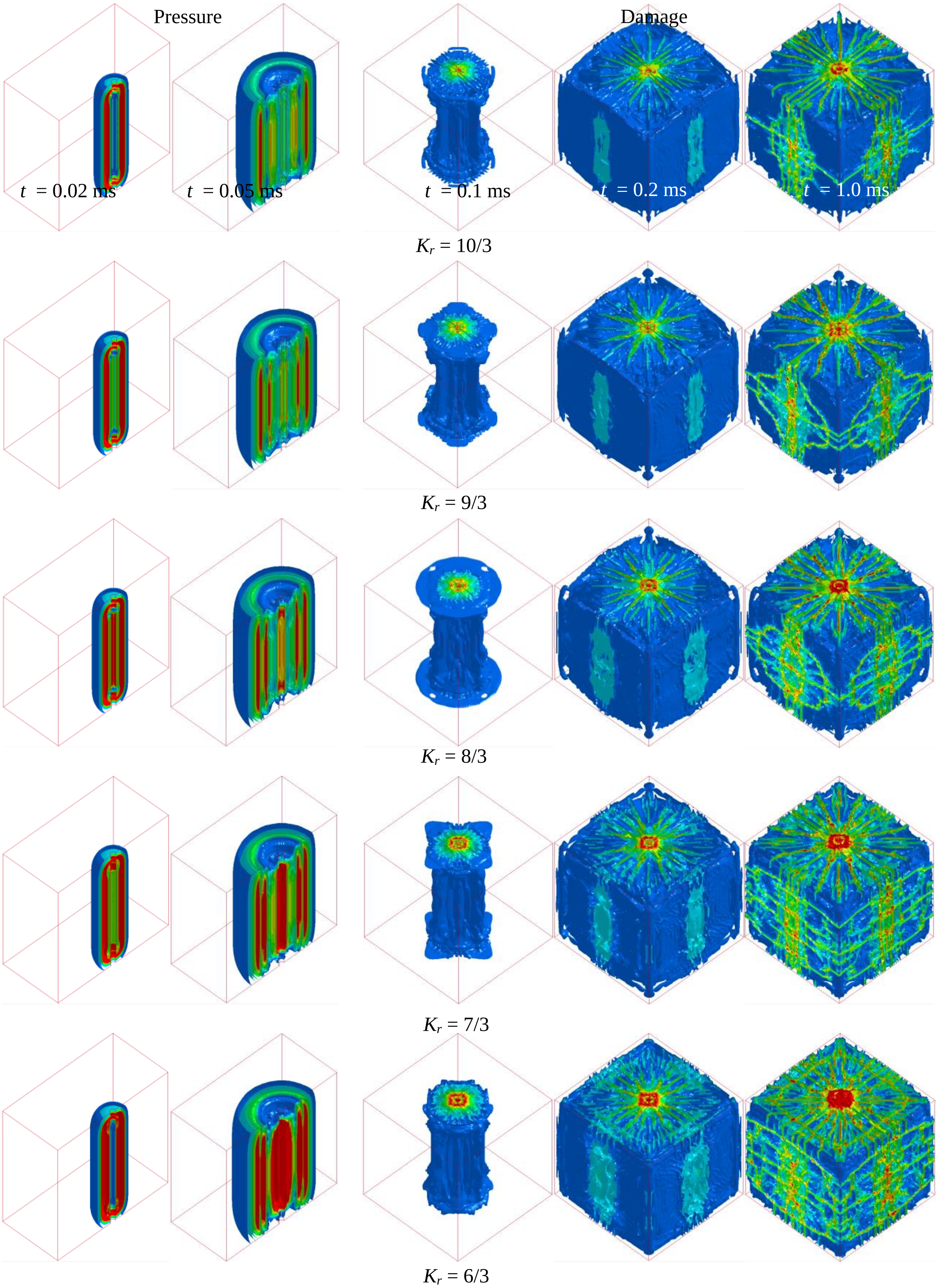

Pressure
Damage
t = 0.02 ms
t = 0.05 ms
t = 0.1 ms
t = 0.2 ms
t = 1.0 ms
K_r = 10/3
K_r = 9/3
K_r = 8/3
K_r = 7/3
K_r = 6/3

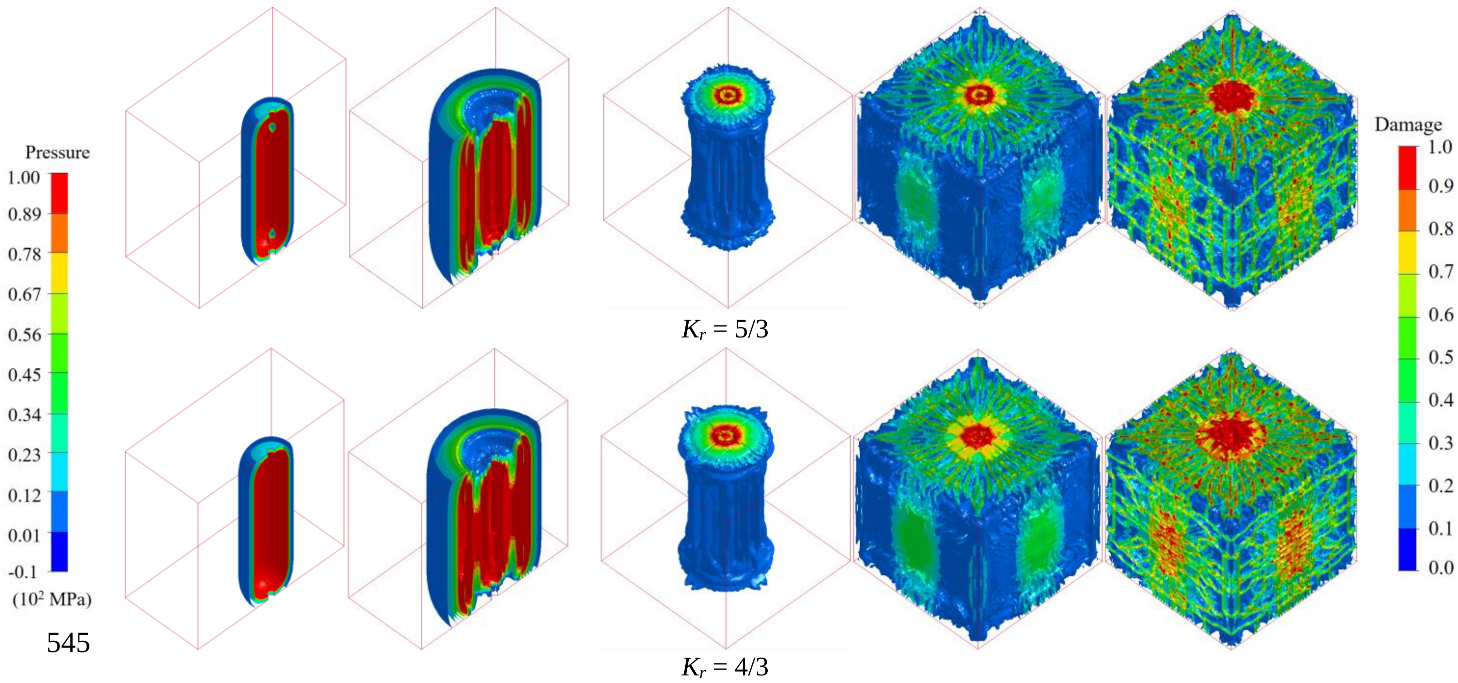

(b)

Fig. 9 Explosion pressure in rock and damage cracks induced by radially decoupling blasting with (a) air coupling and (b) water coupling

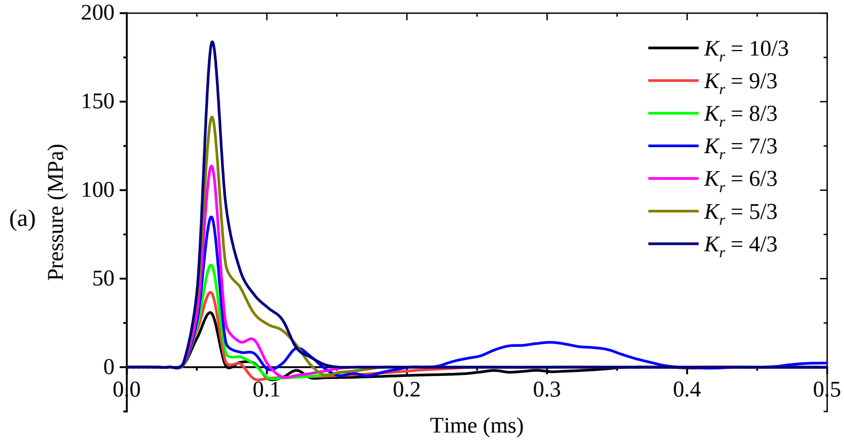

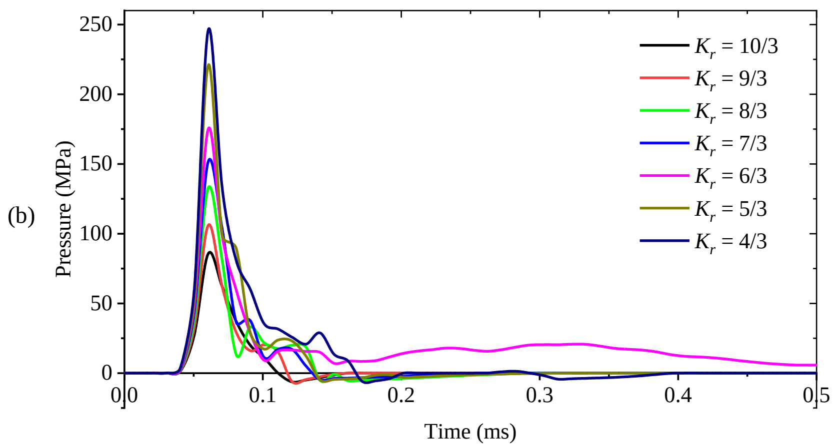

Fig. 10 Time-history curves of explosion pressure at target point (0.25, 0, 0.5/m) induced by radially decoupling blasting with (a) air coupling and (b) water coupling

The final damage patterns induced by radially decoupled charge blasting (opaque view with mesh) and corresponding fracture networks are presented in Fig. 11. It is apparent that the changes in the charge diameter and coupling medium exert a significant influence on the development of blast-induced fractures. In the cases of air-coupling blasting, as shown in Fig. 11(a), the numbers of radial cracks and vertical cracks (cracks propagating in the z direction) increase with the decrease of decoupling ratio due to the increased explosion energy. To be more specific, as the air-filled borehole detonates with K_r = 10/3, four main radial cracks develop in the rock and two mutually perpendicular cutting surfaces are formed. Consequently, this cubic rock block is uniformly cut into four big fragments (quarter cube). When the charge diameter increases, the number of radial cracks raises, and in the range of $8/3 < K_r \leq 10/3$, the cracking patterns in different planes vertical to borehole axial are almost identical, i.e., the blast-created rock fracture is in the form of radiation-shape cracking. Then, as the decoupling ratio continuously decreases from 7/3 to 4/3, the crushed zone expands rapidly and more radial and vertical cracks initiate and propagate in the rock. Meanwhile, the blast-induced cracks propagating in the radial direction and axial direction interact with each other, forming massively developed rock cracks. Especially in the air-coupled blasting with K_r = 4/3, the blast-induced fractures massively develop inside the rock three-dimensionally and thus disintegrate the rock with a large number of small fragments.

In contrast to air-coupled blasting, massively developed cracking is the main fracturing form in water-coupling blasting, as shown in Fig. 11(b), and much more cracks including radial cracks and vertical cracks are created after the detonation of water-filled borehole, implying that smaller rock fragment size is generated. Besides, it is noted that the discrepancy in rock breakage under water-coupling blasting with different decoupling coefficients is less obvious compared with that under air-coupling blasting, indicating that the performance of water-coupling blasting is more robust to the change in charge diameter than that of air-coupling one. Furthermore, with the decrease in decoupling ratio, the difference in the rock fracture between air-coupled blasting and water-coupled blasting becomes smaller due to the thickness reduction of the coupling medium. Obviously, the extent of blast-induced fracture is jointly controlled by the characteristics and thickness of the coupling material.

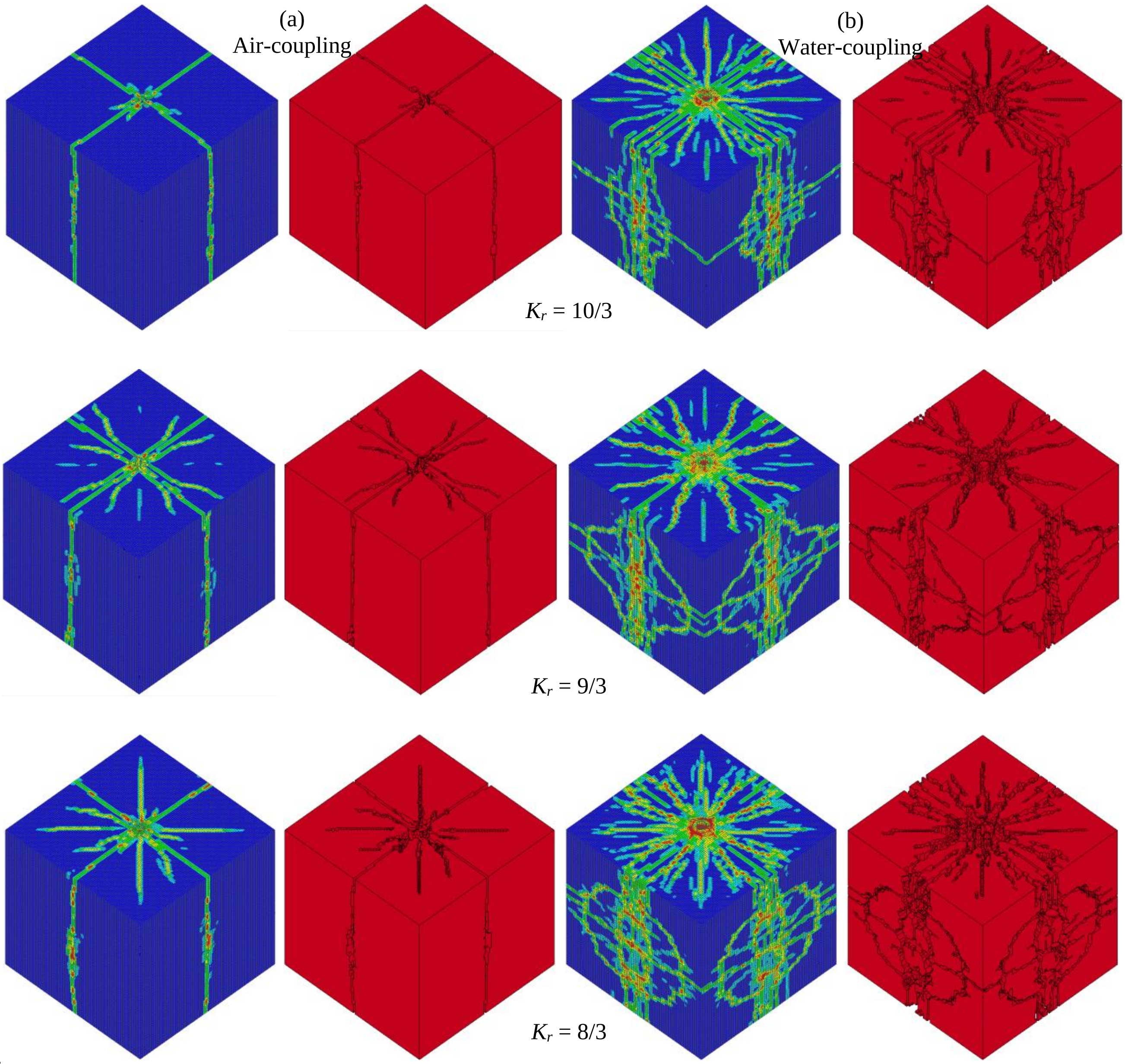

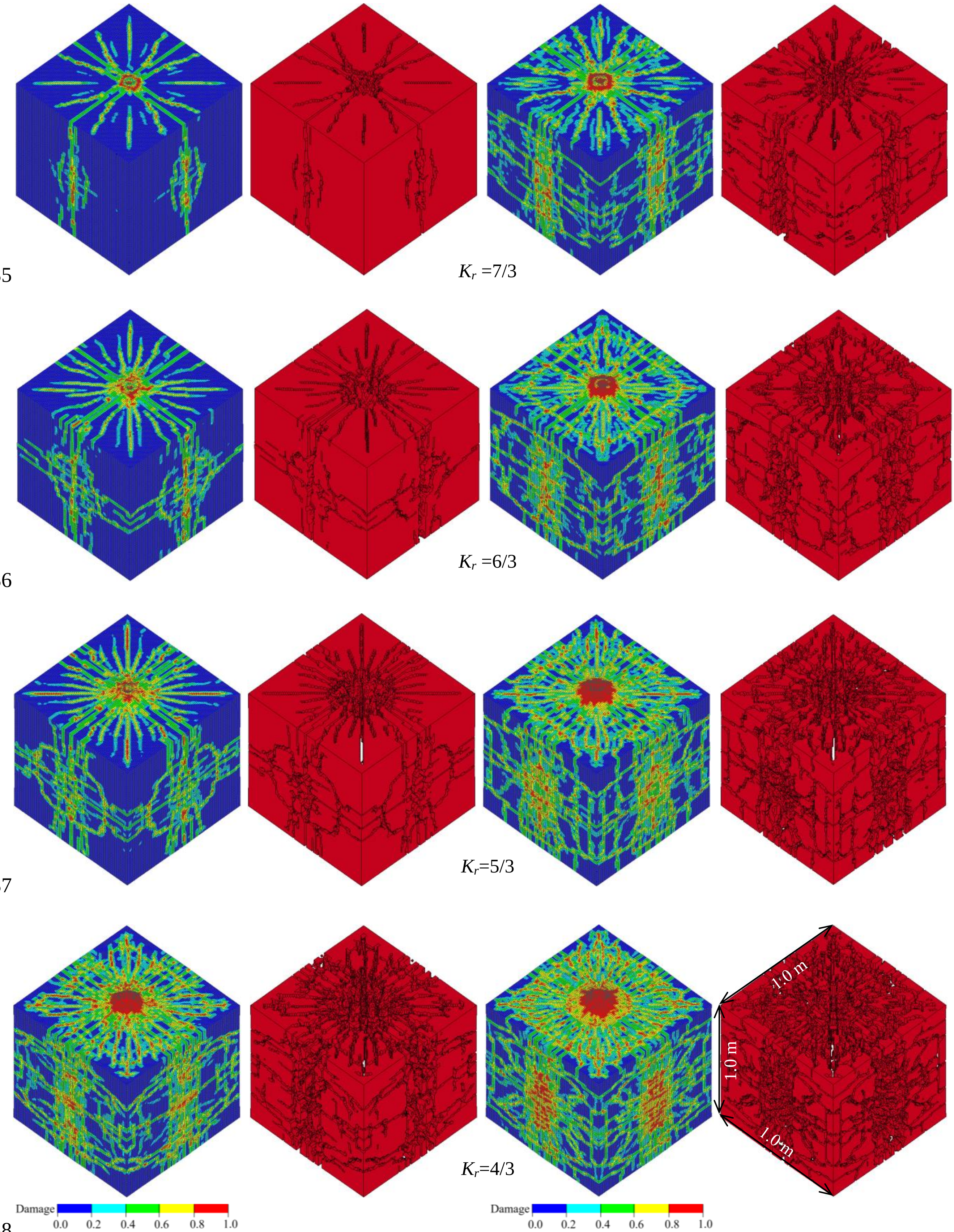

Fig. 11 Damage patterns and fracture networks induced by radially decoupling blasting with (a) air coupling and (b) water coupling

It is acknowledged that when the explosion energy per unit volume increases, more fractures and cracking surfaces in rock are created in rock due to the violent dissipation of dynamic loading energy. At the same time, the steady growth of radial cracks is gradually replaced by the disordered development of 3D crack branching. As can be seen from Fig. 11, as the explosive mass in borehole increases, i.e. with the decrease of decoupling ratio, the cracking form induced by air-coupled blasting varies due to the increased explosion energy density acting on borehole wall. When the air-coupled borehole is detonated with a large decoupling ratio, the rock fracturing is mainly controlled by a few radial cracks, which can generate smooth excavation surfaces parallel to the borehole axial and is beneficial to controlled blasting. In fact, in controlled blasting such as presplitting and smoothwall blasting, lightly radial charged hole is widely adopted for the creation of smooth excavation perimeter (Hu et al. 2014, 2018; Singh et al. 2014). However, when increasing the charge diameter or filling the hole with water, the fracturing form changes from radial cracking to massively developed cracking, and thus the efficiency of rock fragmentation significantly improves, which is conducive to rock excavation in production blasting. These findings are similar to the observations in laboratory-scale blasting tests conducted by Chi et al. (2022). Additionally, in the actual blasting, small decoupling ratio and water coupling are commonly employed to improve the rock fragmentation performance (Huo et al. 2020; Jang et al. 2018).

The cumulative frequency distributions of rock fragmentation obtained in radially decoupled charge blasting via the combined finite element modelling and image-processing and the corresponding fitting curves using the three-parameter GEV function are presented in Fig. 12. It can be seen that the GEV function matches the data of FSDs created by decoupled charge blasting with good accuracy. With the reduction of decoupling ratio, the fitting curves rise earlier, and the size of the biggest fragment decrease, which implies that the rock fragment size gradually shifts toward finer dimension with a more uniform distribution. Furthermore, by comparing the FSDs generated by air and water coupling blasting, it can be indicated that with the same decoupling ratio, smaller fragment size and more uniform FSD is formed under water-coupling blasting, which is consistent with the observations in numerical results shown in Fig. 11 and the findings in the experiments of Chi et al. (2022).

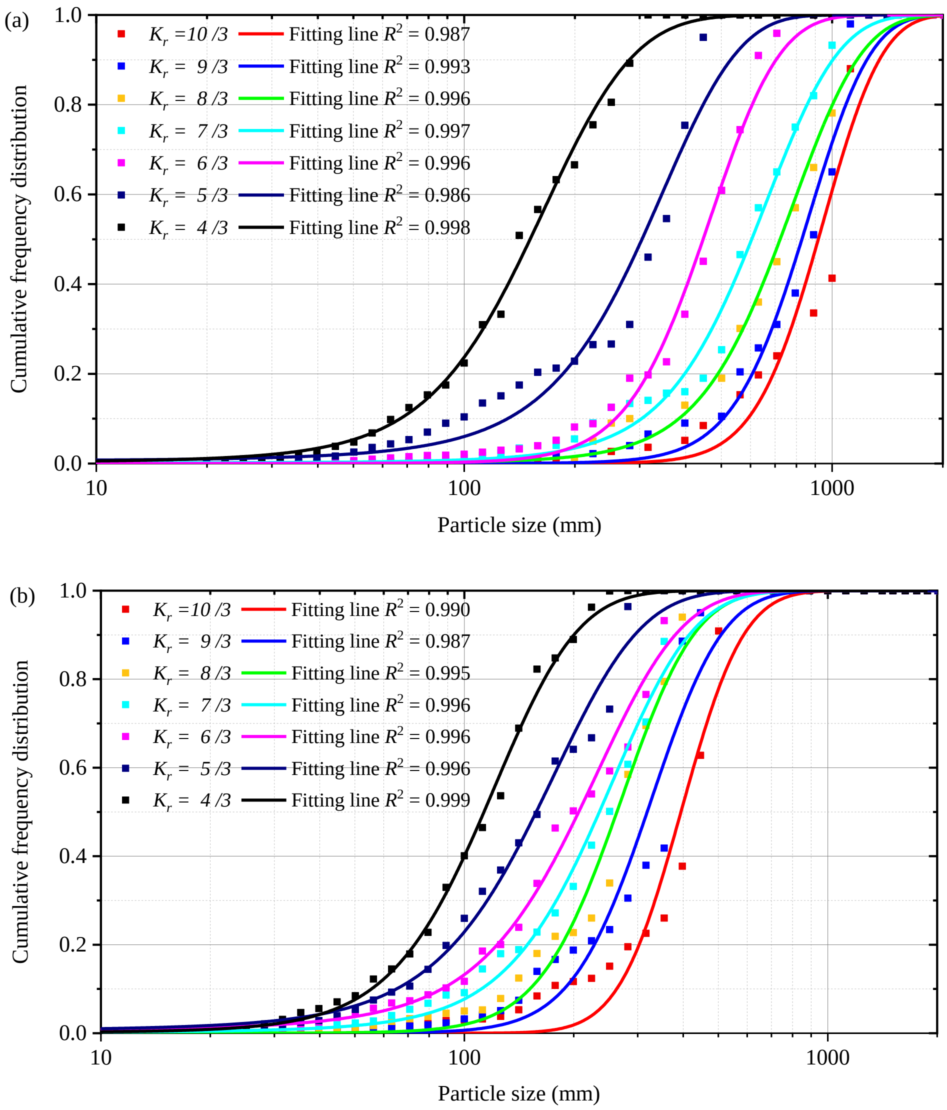

Fig. 12 FSDs and corresponding fitting curves in radially decoupled charge blasting with (a) air coupling and (b) water coupling

3.3. Rock fragmentation induced by axially decoupled charge blasting

Then, the influences of axially decoupled charges on rock fragmentation are numerically examined with different decoupling ratios and distinct coupling mediums, and the processes of explosion pressure evolution and damage crack propagation induced by axially decoupling blasting are given using transparent view in Fig. 13. Different from radially decoupled charge blasting, after detonation, ellipsoidal explosion pressure radiates outward from the position of explosive, and the blast-induced damage zone is also ellipsoidal in the early stage of blast-induced damage evolution, especially in blasting with a large decoupling ratio. Then, radiation-shape cracks propagating from the position of explosive develop outwards and finally cross through the whole rock. During the development of radiation-shape cracks from the detonation point, spalling damage is formed in the vicinity of surface and interacts with radiation-shape cracks. Moreover, the corresponding time-history curves of explosion pressure at target point are presented in Fig. 14. Similar to decoupled charge blasting using radially decoupled charge, the explosion pressure peak increases with the decrease of decoupling ratio, and water-coupling produces higher explosion pressure. But with the same decoupling ratio and coupling medium, the explosion pressure peak in axially decoupled charge blasting is higher. Besides, a smaller difference in pressure peak between air-coupling blasting and water-coupling blasting is found in axially decoupled charge blasting.

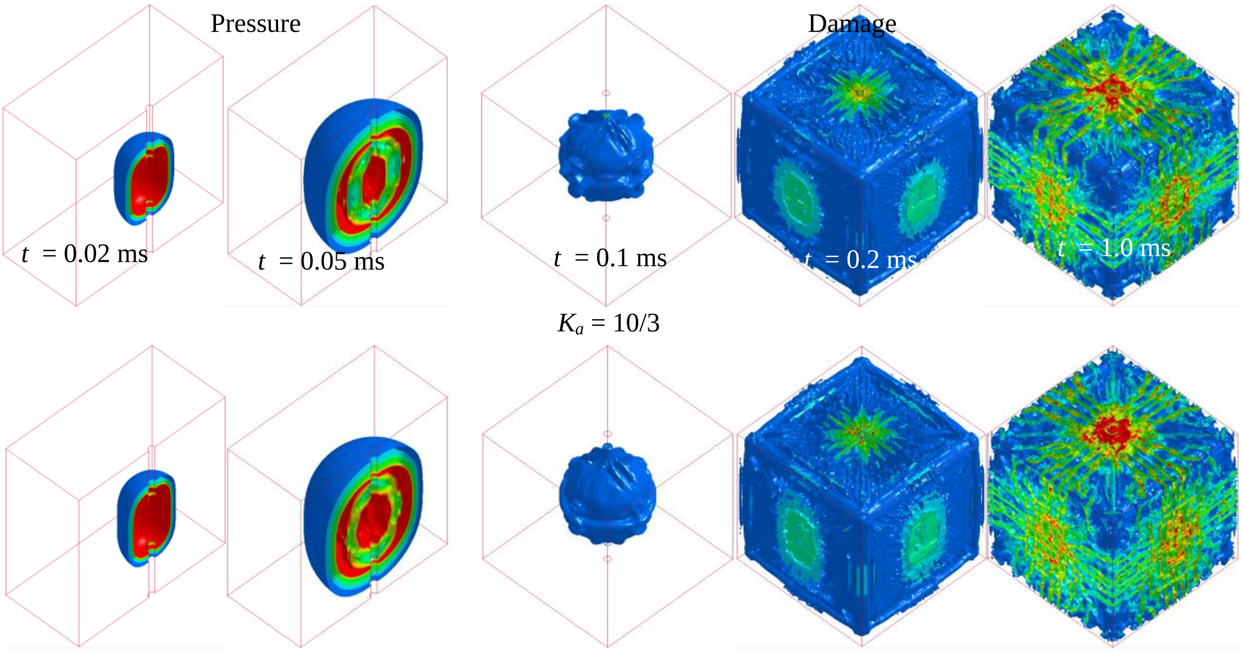

K_a = 9/3

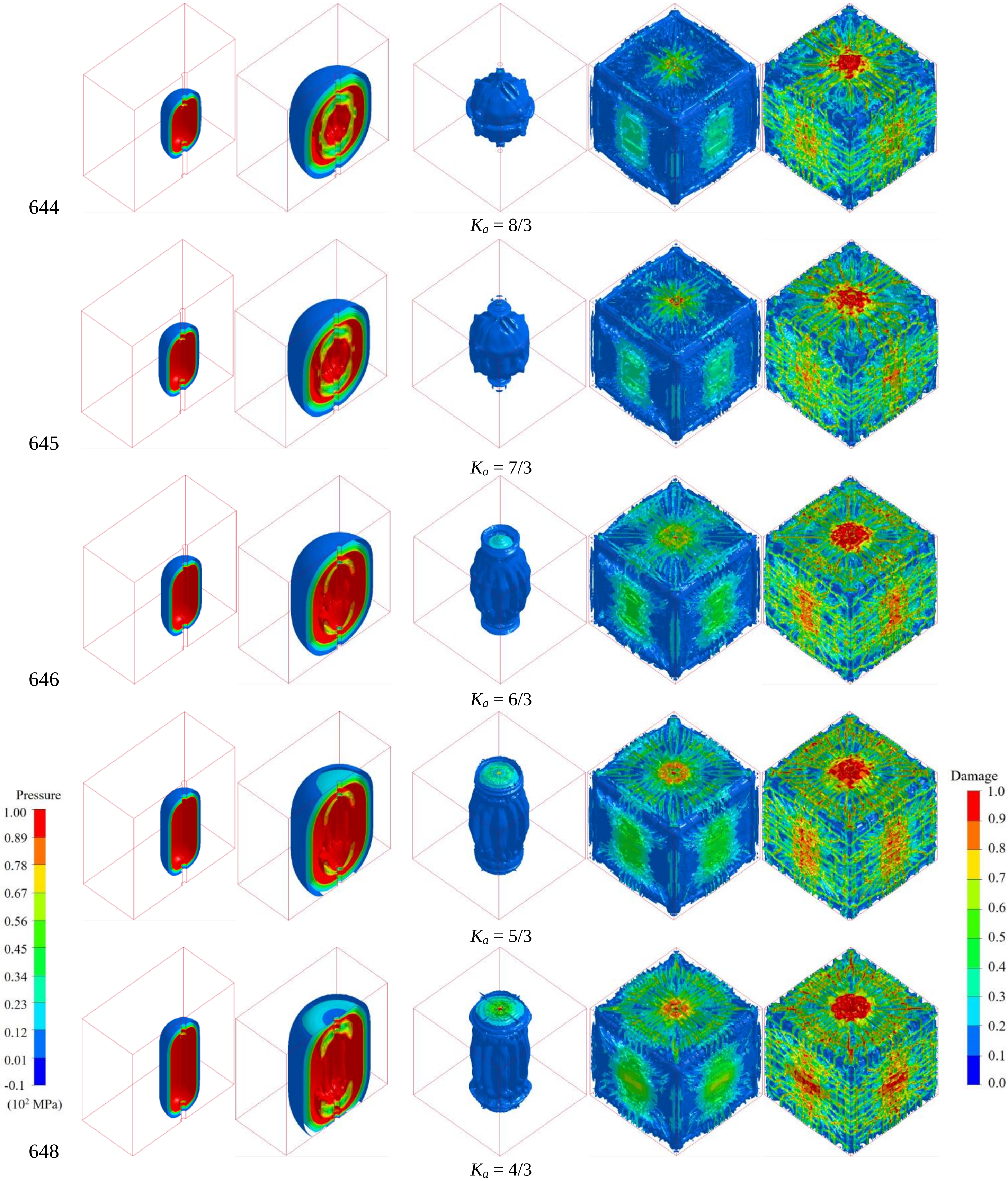

K_a = 8/3
K_a = 7/3
K_a = 6/3
K_a = 5/3
K_a = 4/3
Pressure
1.00
0.89
0.78
0.67
0.56
0.45
0.34
0.23
0.12
0.01
-0.1
(10^2 MPa)
Damage
1.0
0.9
0.8
0.7
0.6
0.5
0.4
0.3
0.2
0.1
0.0

(a)

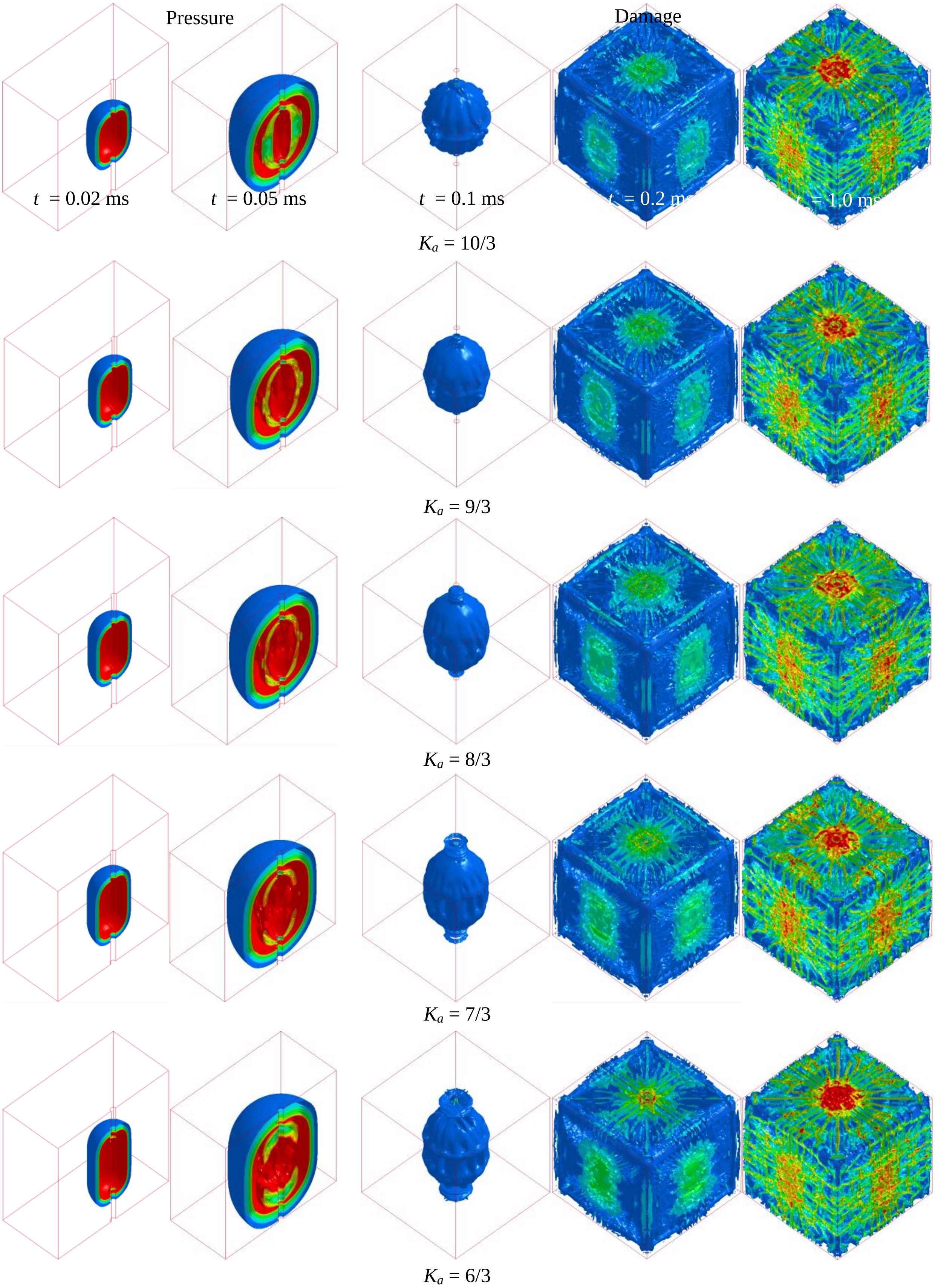
Pressure
Damage
t = 0.02 ms
t = 0.05 ms
t = 0.1 ms
t = 0.2 ms
t = 1.0 ms
K_a = 10/3
K_a = 9/3
K_a = 8/3
K_a = 7/3
K_a = 6/3

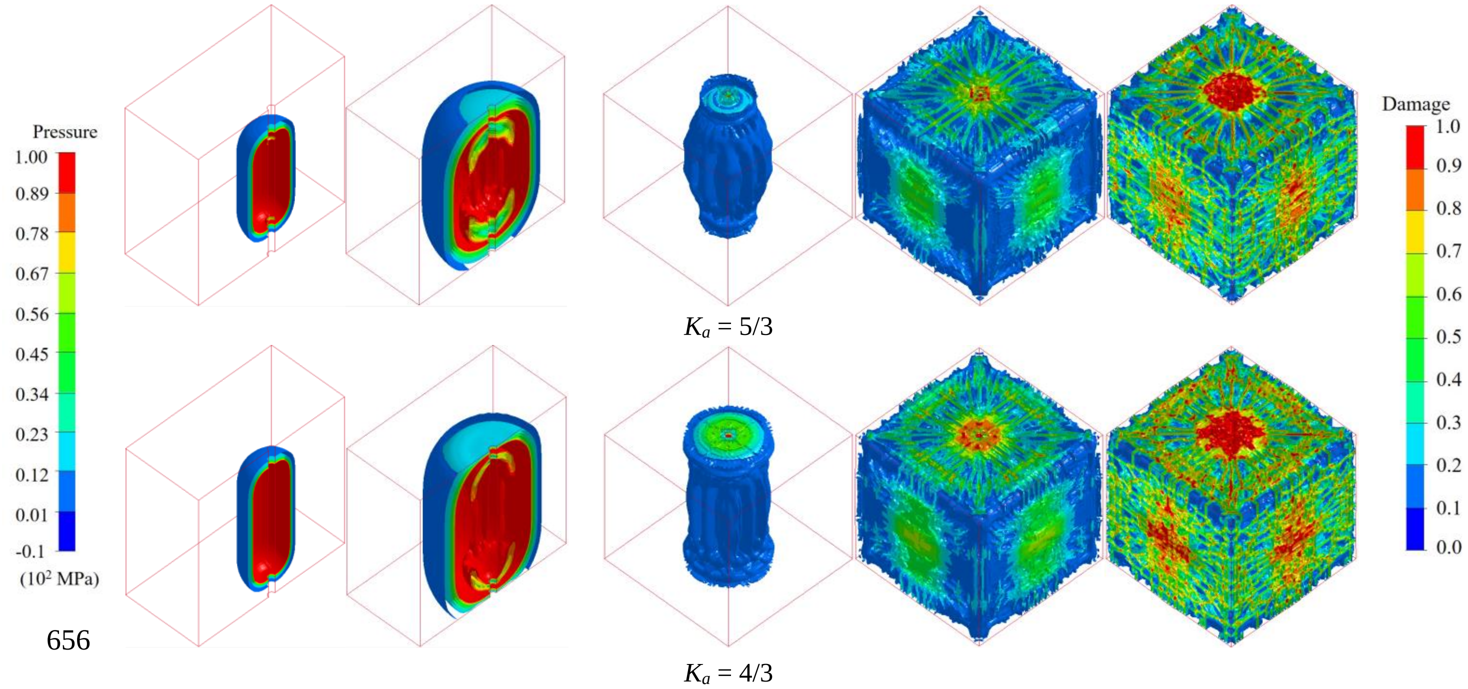

(b)

Fig. 13 Explosion pressure in rock and damage cracks induced by axially decoupling blasting with (a) air coupling and (b) water coupling

(a)

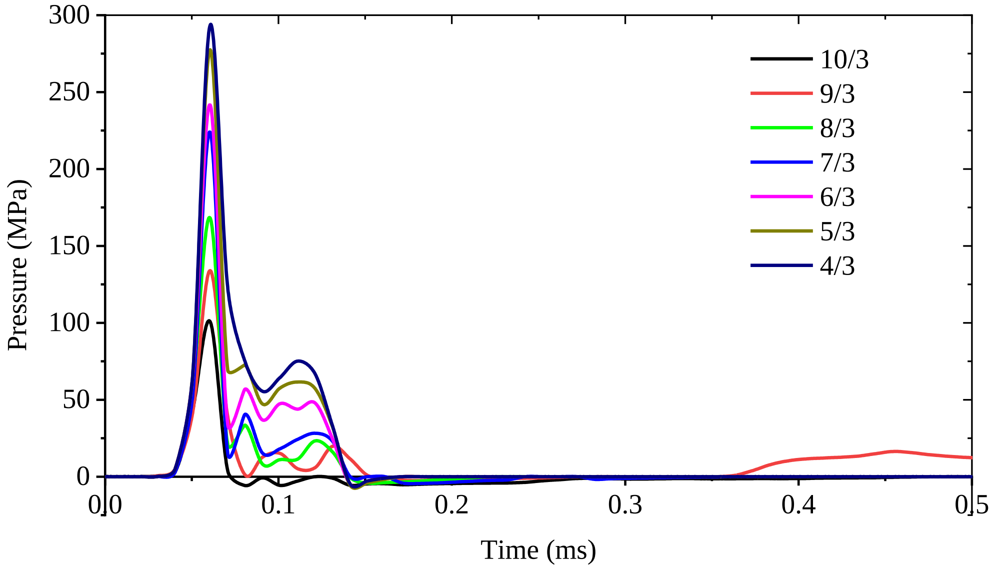

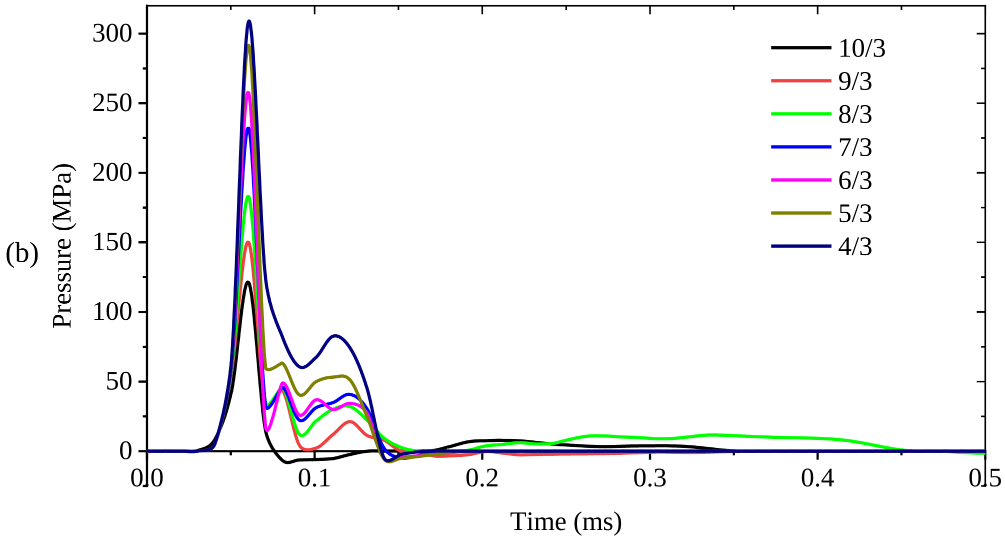

Fig. 14 Time-history curves of explosion pressure at target point (0.25, 0, 0.5/m) induced by axially decoupling blasting with (a) air coupling and (b) water coupling

The damage patterns using opaque view and corresponding fracture networks are shown in Fig. 15. In consistency with blasting with radially decoupled charge, the extent of rock fracture gradually becomes higher as the decoupling ratio decreases, and the rock disintegration under air-coupling blasting is slighter than that under water-coupling blasting. These findings also agree with the simulated explosion pressure presented in Fig. 14. Besides, the rock fracturing under water-coupling blasting with different decoupling coefficients shows a smaller difference compared with that under air-coupling blasting. This can be expected since the difference in explosion pressure peak between air-coupling blasting and water-coupling blasting in axially decoupled charge blasting is smaller than that in radially decoupled charge blasting, as can be compared and found between Fig. 10 and Fig. 14. However, in the cases of axially decoupled charge blasting, massively developed cracks are created in all air-coupling and water-coupling blasts, which increases the potential for the formation of finer fragments. Moreover, the difference in rock cracking induced by blasting with various decoupling ratios and the discrepancy in rock fracture with different coupling mediums are much smaller compared with those in radially decoupled charge blasting, implying a small dependence of rock fracturing on decoupling coefficient and coupling material in axially decoupled charge blasting.

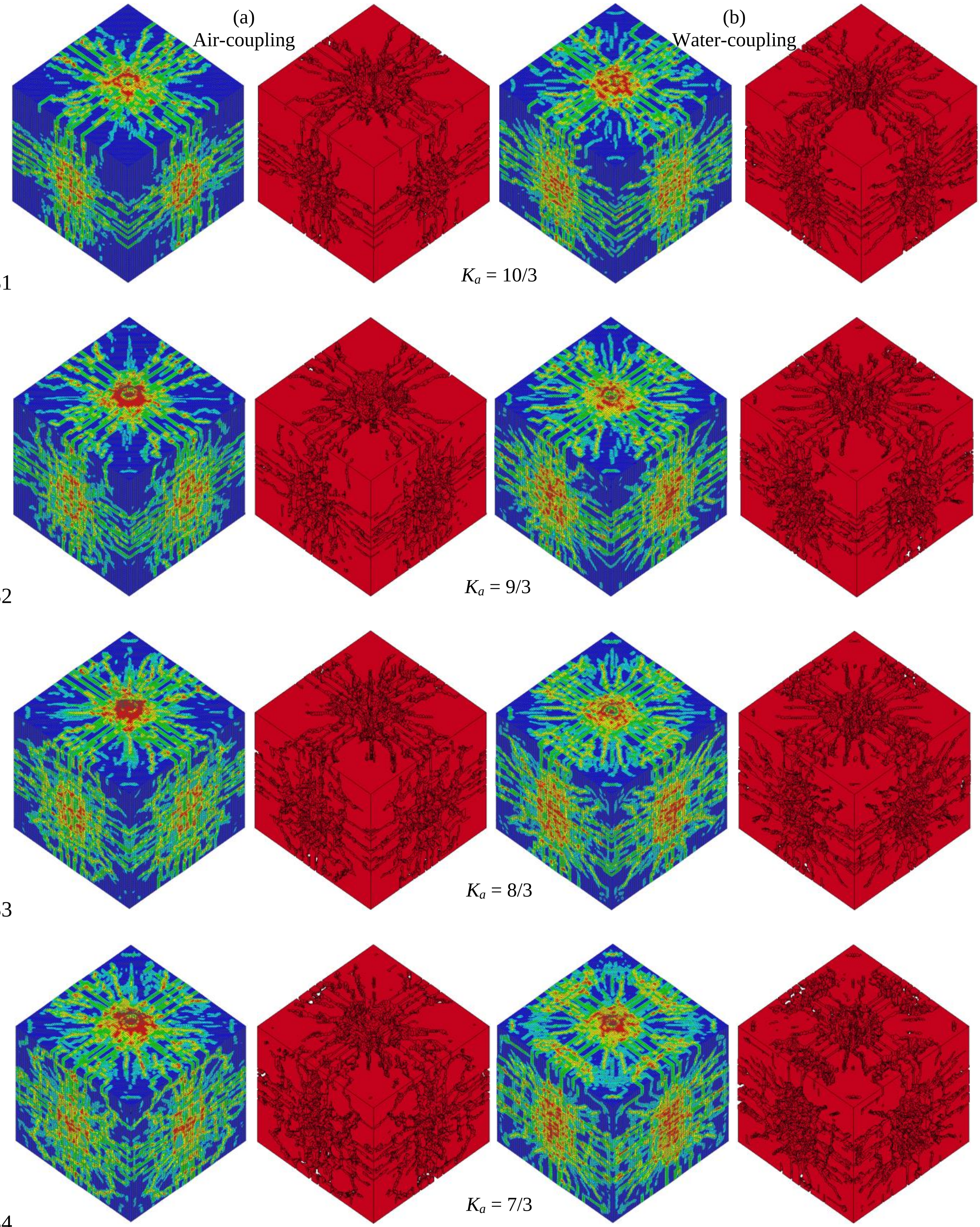

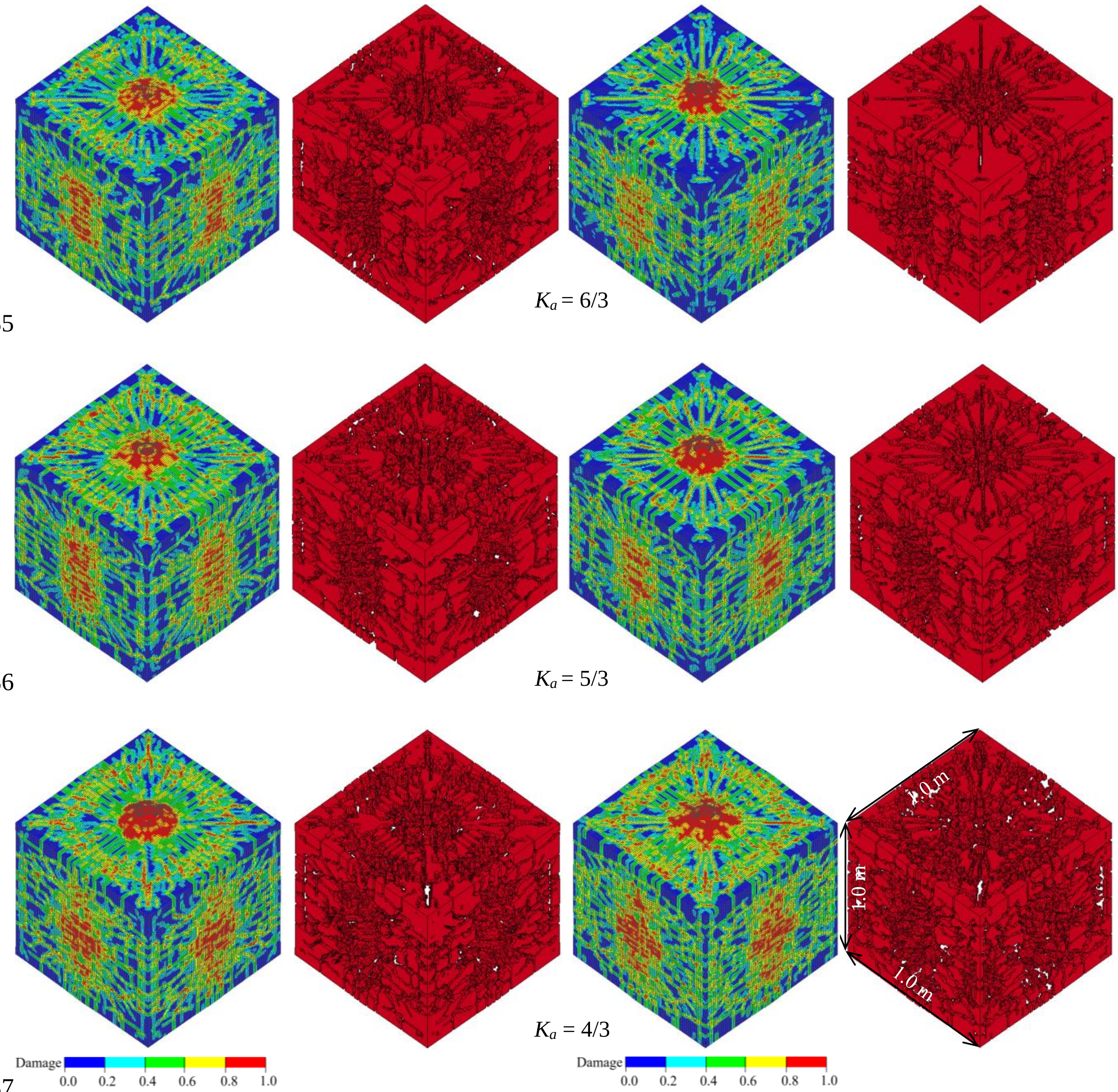

Fig. 15 Damage patterns and fracture networks induced by axial decoupling blasting with (a) air coupling and (b) water coupling

Furthermore, the biggest difference between radially decoupled blasting and axially decoupled blasting is the extent of rock fracture. It can be easily observed by comparing Fig. 11 and Fig. 15 that the rock cracking under axial decoupling blasting is greatly intensified compared with that under radial decoupling one. This is the result that the explosion pressure peak induced by axially decoupled charge blasting is higher than radially decoupled charge one, as shown in Fig. 10 and Fig. 14, and it is attributed to the existence of explosive-rock interface when using axially decoupled charge mode. In other words, the direct contact between explosive and rock greatly enhances the energy transmission from explosion products into rock mass. Therefore, in practice, a gap between explosive and hole-wall filling coupling medium is considerably necessary for alleviating damage to surrounding rock, and the charge structure of direct contact is important and highly efficient to facilitate the growth of rock fractures. In controlled blasting, lightly loaded boreholes with air-coupling should be employed for the stability of the remaining rock, while the axially decoupled charge or decked charge with water-coupling can be adopted to fragment rock with high efficiency and cut down the consumption of explosive in production blasting.

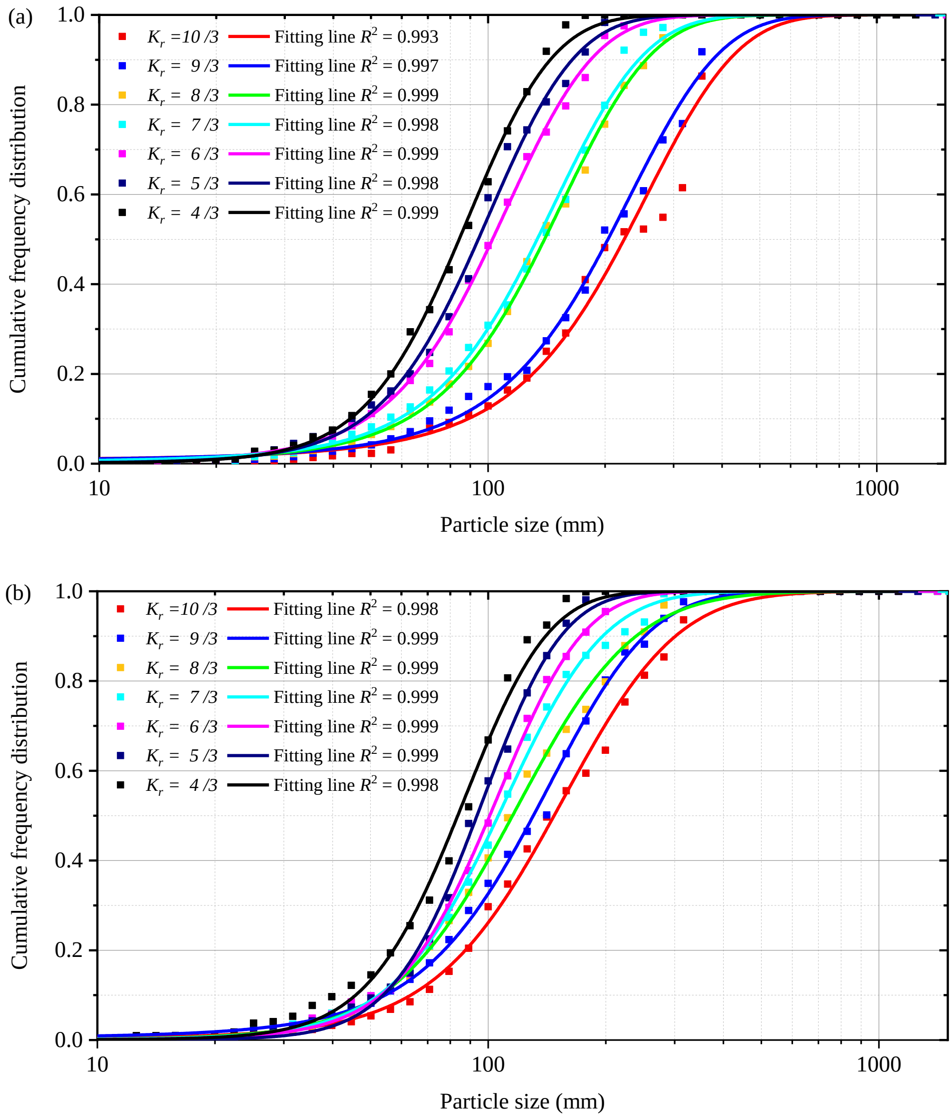

Fig. 16 FSDs and corresponding fitting curves using the three-parameter GEV function under axially decoupled charge blasting with (a) air coupling and (b) water coupling

Figure 16 shows the resulting cumulative frequency distributions of rock fragmentation induced by axially decoupled charge blasting and the corresponding fitting curves. Some data that show relatively large discrepancy against the fitted curve among others are induced by insufficient fragmentation, i.e., oversize fragmentation. Similar discrepancy can be found in Fig. 12, especially for data of blasting with a large decoupling ratio, due to the same reason. It can be seen that the fitting curves rise later with a larger decoupling ratio, and at the same decoupling coefficient, the fitting curve for cumulative frequency distribution generated by air-coupling blasting rises later than that of water-coupling one. These results also indicate that under axially decoupled charge blasting, finer fragments and more uniform FSDs are generated with the increase of charge length, i.e. the increase of explosion energy. Moreover, air-coupling blasting creates coarser fragments and more scattering FSD due to the lower efficiency in stress transmission of air. Compared with FSDs obtained in radially coupled charge blasting, in both air and water coupling blasts, finer fragment size and narrower range of FSD are formed in blasting with axially decoupled charge, indicating a growing number of small fragments and a decreasing size difference between large fragments and fine fragments upon changing the charge mode from radial decoupling to axial decoupling. This finding means that the axially decoupled charge mode is more efficient in the energy transmission from explosive to rock mass.

4. Discussion

It has demonstrated in the present numerical modelling and image processing that the fragment size and the FSD range under blasting with various coupling mediums and different decoupled charge modes respond similarly to the change of decoupling ratio. However, the rates at which the fragment size and the FSD span change are markedly different among these cases of blasting. Figures 17(a) and 17(b) show the variations of the parameters μ and σ of the GEV distribution with respect to the increase of decoupling ratio, which scale with the average size and size distribution range of the rock fragment, respectively. These plots show that both the parameters of μ and σ increase with the increase of decoupling ratio, suggesting an overall increase of the fragment size and broadening of the distribution span with the reduction of charge amount. Moreover, with the same decoupling ratio, larger μ and σ are obtained under basting with axial decoupling than their counterparts with radial decoupling, and higher values of μ and σ are gotten in blasting with water-coupling, indicating that changing charge mode from axial decoupling to radial decoupling and replacing coupling material water with air play extremely remarkable roles in increasing overall fragment size and broadening the range of FSD.

It can be found in Fig. 17 that both the parameters of μ and σ show a linearly increasing trend with the increase of the decoupling coefficient. By linear fitting parameters of μ and σ, the effects of decoupling ratios on the average size and distribution span of rock fragments with different coupling mediums and decoupled charge modes can be quantitatively evaluated by the corresponding slopes. Obviously, the slopes of μ and σ with radial air-coupling are much higher than those with axial decoupling and water-coupling, and they have the lowest value in the case of axial water-coupling, suggests that the overall fragment size and the FSD range are the most and the minimal sensitive to the change of decoupling coefficient under radial air-coupling blasting and axial water-coupling blasting, respectively. Under this situation, the extent of crack fracture can be easily controlled in blasting with radial air-coupling such that the formation of smooth excavation surface in controlled blasting can be achieved by adjusting charge diameter. In comparison, the consumption of explosive can be significantly cut down in production blasting using the charge configuration of axial water-coupling.

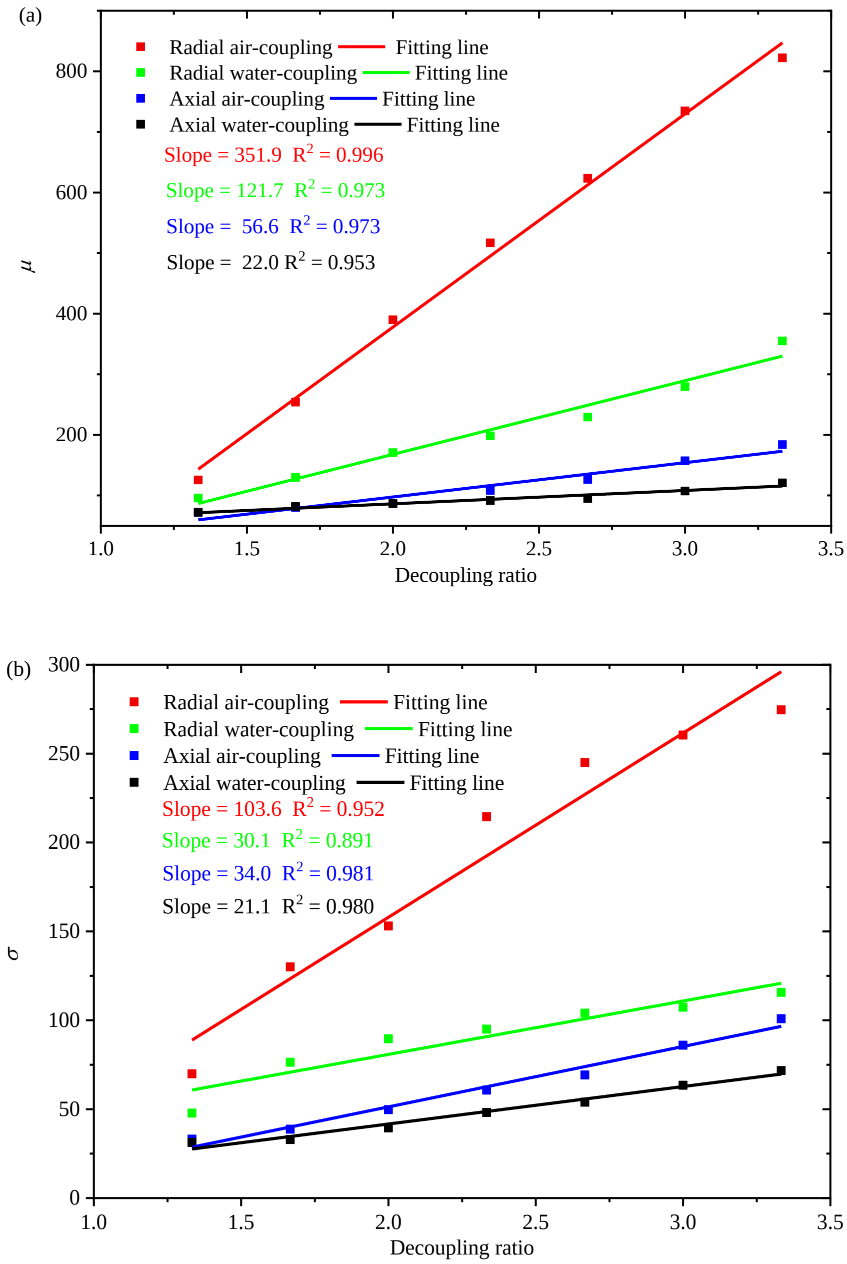

Fig. 17 Variations of fragment parameters with the increase of decoupling ratio: (a) μ; (b) σ

The fragment size and FSD range also show a linear relationship, and the linear fitting line of μ vs. σ is plotted in Fig. 18. This linear correlation suggests that the distribution range of fragment size broadens with the increase of average fragment size and can be explained as follows: with the increase of decoupling ratio, altering water-coupling to air-coupling or adjusting axial decoupling to radial decoupling, the explosion energy transmitted from explosive to rock mass decreases, which consequently lead to the creation of larger fragments.

Due to the increase in the overall fragment size, the difference between oversize fragments and small or fine particles gets larger, which eventually gives rise to the formation of a broader FSD range. The strong correlation in Fig. 18 indicates that both the parameters of μ and σ can serve as valuable indicators of fragmentation efficiency. The smaller values of μ and σ imply the better performance of rock fragmentation in decoupling charge blasting.

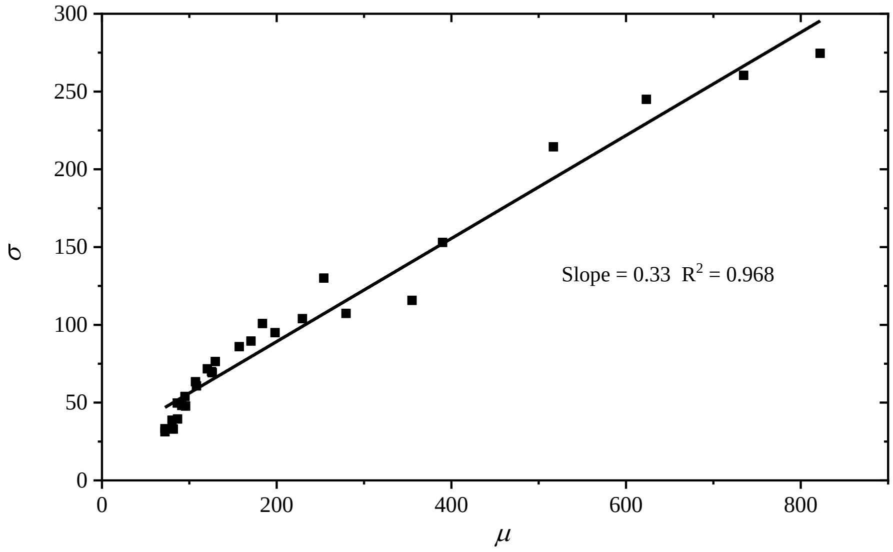

Fig. 18 Correlations between the fragment size and FSD range

5. Conclusions

In this study, the rock fragmentation induced by decoupled charge blasting is systematically investigated with the changes in decoupling ratio, coupling medium and decoupled charge mode by combining finite element simulation and image processing. Based on the numerical findings and data analysis, the following conclusions can be drawn:

Parameters for rock, explosive and coupling materials in numerical modelling are determined based on basic rock mechanical parameter, theoretical calculation and reference, and the currently developed numerical model is suitable and applicable for modelling rock fragmentation induced by decoupled charge blasting using air-coupling and water-coupling with free surfaces. The fracture networks in simulation are obtained by blanking the damaged elements whose damage level is over the threshold of crack formation, and the rationality of this method is verified by comparing the simulated crack pattern and experimental fragment morphology.

In blasting with radial air-coupling, the rock fracturing varies from radiation-shape fracture pattern to massively developed rock cracks with the decreasing of decoupling ratio, whereas 3D cracking is the main fracturing form in water-coupling and axial decoupling blasts. The blast-induced rock fragmentation becomes finer and the FSD range gets narrower with the decrease of decoupling ratio. Meanwhile, smaller fragment sizes and narrower FSD spans are formed when changing coupling material from air to water and altering radial decoupling to axial decoupling. The overall fragment size and the FSD range have the highest and the minimal sensitivity to the change of decoupling coefficient under radial air-coupling blasting and axial water-coupling blasting, respectively. Coarser fragments lead to a broader FSD range. The strong correlation between the fragment size and FSD range highlights that the parameters of μ and σ can serve as valuable indicators of fragmenting efficiency.

CRediT authorship contribution statement

Xudong Li: Conceptualization, Investigation, Writing - Original Draft. **Kewei Liu**: Supervision, Methodology, Writing - review & editing. **Yanyan Sha**: Supervision, Writing - review & editing. **Jiacai Yang**: Validation. **Ruitao Song**: Writing – review & editing.

Acknowledgments

The authors acknowledge the financial support from the National Natural Science Foundation of China under Grant no. 51974360 for carrying out this research work.

References

An, H.M., Liu, H.Y., Han, H., Xin, Z., Wang, X.G., 2017. Hybrid finite-discrete element modelling of dynamic fracture and resultant fragment casting and muck-piling by rock blast. Comput. Geotech. 81, 322-345. https://doi.org/10.1016/j.compgeo.2016.09.007.

Banadaki, M.M.D., 2010. Stress-wave induced fracture in rock due to explosive action. University of Toronto, Scarborough, Canada.

Baranowski, P., Mazurkiewicz, L., Malachowski, J., Pytlik, M., 2020. Experimental testing and numerical simulations of blast-induced fracture of dolomite rock. Meccanica. https://doi.org/10.1007/s11012-020-01223-0.

Bobaru F.,·Zhang, G.F., 2016. Why do cracks branch? A peridynamic investigation of dynamic brittle fracture. Int. J. Fract. https://doi.org/10.1007/s10704-015-0056-8.

Borrvall, T., Riedel, W., 2011. The RHT concrete model in LS-DYNA. Proceedings of The 8th European LS-DYNA user conference.

Brannon, R.M., Leelavanichkul, S., 2009. Survey of four damage models for concrete. Sandia National Laboratories. 1–80. https://doi.org/10.2172/993922.

Chen, M., Ye, Z.W., Lu, W.B., Wei, D., Yan, P., 2020. An improved method for calculating the peak explosion pressure on the borehole wall in decoupling charge blasting. Int. J. Impact. Eng. 146(103695. https://doi.org/10.1016/j.ijimpeng.2020.103695.

Chi, L.Y., Wang, C., Zhang, Z.X., Xu, X., Yang, J., 2022. Experimental investigation of decoupled charge effect on rock fragmentation by blasting. Rock. Mech. Rock. Eng. 55, 3791-3806. https://doi.org/10.1007/s00603-022-02823-w.

L. S. T. C., 2015. LS-DYNA keyword user's manual. Version R 8.0 (Livermore CA).

Cui, Z.D., Yuan, L., Yan, C.L., 2010. Water–silt composite blasting for tunneling. Int. J. Rock. Mech. Min. Sci. 47(6), 1034-1037. https://doi.org/10.1016/j.ijrmms.2010.06.004.

Dehghani, H., Babanouri, N., Alimohammadnia, F., Kalhori, M., 2020. Blast-induced rock fragmentation in wet holes. Mining. Metall. Explor. 37(2), 743-752. https://doi.org/10.1007/s42461-019-00163-y.

Diehl, A., Carmona, H., Araripe, L., Andrade J. J., Farias, G., 2000. Scaling behavior in explosive fragmentation. Phys Rev E. 62(4). https://doi.org/10.1103/PhysRevE.62.4742.

Ding, C., Yang, R., Lei, Z., Wang, M., Lin, H., 2020. Fractal damage and crack propagation in decoupled charge blasting. Soil. Dyn. Earthq. Eng. 141(106503). https://doi.org/10.1016/j.soildyn.2020.106503.

Durda, D.D., Bagatin, A.C., Alemañ, R.A., Flynn, G.J., Strait, M.M., Clayton, A.N., Patmore, E.B., 2015. The shapes of fragments from catastrophic disruption events: effects of target shape and impact speed. Planet. Space. Sci. 107, 77-83. https://doi.org/10.1016/j.pss.2014.10.006.

Fourney, W.L., Barker, D.B., Holloway, D.C., 1981. Model studies of explosive well stimulation techniques. Int. J. Rock. Mech. Min. Sci. 18(2), 113-127. https://doi.org/10.1016/0148-9062(81)90737-3.

Gharehdash, S., Barzegar, M., Palymskiy, I.B., Fomin, P.A., 2020. Blast induced fracture modelling using smoothed particle hydrodynamics. Int. J. Impact. Eng. 135, 103231-103235. https://doi.org/10.1016/j.ijimpeng.2019.02.001.

Green, L., Lee, E., 2006. Detonation pressure measurements on PETN. Proceedings of 13th International Detonation Symposium.

Han, H., Fukuda, D., Liu, H., Salmi, E.F., Sellers, E., Liu, T., Chan, A., 2020. Combined finite-discrete element modelling of rock fracture and fragmentation induced by contour blasting during tunnelling with high horizontal in-situ stress. Int. J. Rock. Mech. Min. Sci. 127(104214). https://doi.org/10.1016/j.ijrmms.2020.104214.

Hashemi, A.S., Katsabanis, P., 2021. Tunnel face preconditioning using destress blasting in deep underground excavations. Tunn. Undergr. Space. Technol. 117(104126). https://doi.org/10.1016/j.tust.2021.104126.

Hogan, J.D., Rogers, R.J., Spray, J.G., Boonsue, S., 2012. Dynamic fragmentation of granite for impact energies of 6–28 J. Eng. Fract. Mech. 79, 103-125. https://doi.org/10.1016/j.engfracmech.2011.10.006.

Hou, T.X., Xu, Q., Yang, X.G., Lu, P.Y., Zhou, J.W., 2015. Experimental study of the fragmentation characteristics of brittle rocks by the effect of a freefall round hammer. Int. J. Fracture. 194(2), 169-185. https://doi.org/10.1007/s10704-015-0046-x.

Hu, Y.G., Lu, W.B., Chen, M., Yan, P., Yang, J.H., 2014. Comparison of blast-induced damage between presplit and smooth blasting of high rock slope. Rock. Mech. Rock. Eng. 47:1307-1320. https://doi.org/10.1007/s00603-013-0475-7.

Hu, Y.G., Lu, W.B., Wu, X.X., Liu, M.S., Li, P., 2018. Numerical and experimental investigation of blasting damage control of a high rock slope in a deep valley. Eng. Geol. 37:12-20. https://doi.org/10.1016/j.enggeo.2018.01.003.

Huang, B.X., Li, P.F., 2015. Experimental investigation on the basic law of the fracture spatial morphology for water pressure blasting in a drillhole under true triaxial stress. Rock. Mech. Rock. Eng. 48(4), 1699-1709. https://doi.org/10.1007/s00603-014-0649-y.

Huo, X., Shi, X., Qiu, X., Zhou, J., Gou, Y., Yu, Z., Ke, W., 2020. Rock damage control for large-diameter-hole lateral blasting excavation based on charge structure optimization. Tunn. Undergr. Space. Technol. 106(103569). https://doi.org/10.1016/j.tust.2020.103569.

Jang, H., Handel, D., Ko, Y., Yang, H.S., Miedecke, J., 2018. Effects of water deck on rock blasting performance. Int. J. Rock. Mech. Min. Sci. 112, 77-83. https://doi.org/10.1016/j.ijrmms.2018.09.006.

Katsabanis, P.D., 2020. Analysis of the effects of blasting on comminution using experimental results and numerical modelling. Rock. Mech. Rock. Eng. 53(7), 3093-3109. https://doi.org/10.1007/s00603-020-02093-4.

Kutter, H.K., Fairhurst, C., 1971. On the fracture process in blasting. Int. J. Rock. Mech. Min. Sci. 8(3), 181-202. https://doi.org/10.1016/0148-9062(71)90018-0.

Langefors, U., Kihlström, B., 1978. The modern technique of rock blasting. Wiley.

Lee, E.L., Hornig, H.C., Kury, J.W., 1968. Adiabatic expansion of high explosive detonation products, UCRL-50422.

Leng, Z., Sun, J., Lu, W., Xie, X., Jia, Y., Zhou, G., Chen, M., 2021. Mechanism of the in-hole detonation wave interactions in dual initiation with electronic detonators in bench blasting operation. Comput. Geotech. 129(103873). https://doi.org/10.1016/j.compgeo.2020.103873.

Li, X.B., 2014. Rock dynamic fundamentals and applications. Science Press.

Li, X.D., Liu, K.W., Yang, J.C., 2020. Study of the rock crack propagation induced by blasting with a decoupled charge under high in situ stress. Adv. Civ. Eng. (9490807). https://doi.org/10.1155/2020/9490807.

Li, X.D., Liu, K.W., Yang, J.C., Song, R.T., 2022. Numerical study on blast-induced fragmentation in deep rock mass. Int. J. Impact. Eng. 170(104367). https://doi.org/10.1016/j.ijimpeng.2022.104367.

Liang, W., Liu, H., Yang, X., Williams, D., 2011. Effects of decoupled charge blasting on rock fragmentation efficiency. Harmonising Rock Engineering and the Environment.

Liu, K., Li, Q.Y., Wu, C.Q., 2018a. A study of cut blasting for one-step raise excavation based on numerical simulation and field blast tests. Int. J. Rock. Mech. Min. Sci. 109, 91-104.

Liu, K.W., Li, X.D., Hao, H., Li, X.B., Sha, Y.Y., Wang, W.H., Liu, X.L., 2019. Study on the raising technique using one blast based on the combination of long-hole presplitting and vertical crater retreat multiple-deck shots. Int. J. Rock. Mech. Min. Sci. 113, 41-58. https://doi.org/10.1016/j.ijrmms.2018.11.012.

Liu, K.W., Yang, J.C., Li, X.B., Hao, H., Li, Q.Y., Liu, Z.X., Wang, C.Y., 2018b. Study on the long-hole raising technique using one blast based on vertical crater retreat multiple deck shots. Int. J. Rock. Mech. Min. Sci. 109, 52-67. https://doi.org/10.1016/j.ijrmms.2018.06.020.

Luo, Y., Xu, K., Huang, J., Li, X., Liu, T., Qu, D., Chen, P., 2021. Impact analysis of pressure-relief blasting on roadway stability in a deep mining area under high stress. Tunn. Undergr. Space. Technol. 110(103781). https://doi.org/10.1016/j.tust.2020.103781.

Pál, G., Varga, I., Kun, F., 2014. Emergence of energy dependence in the fragmentation of heterogeneous materials. Phys. Rev. E. 90(6). https://doi.org/10.1103/PhysRevE.90.062811.

Pan, C., Xie, L.X., Li, X., Liu, K., Gao, P.F., Tian, L.G., 2022. Numerical investigation of effect of eccentric decoupled charge structure on blasting-induced rock damage. J. Cent. South. Univ. 29(2), 663-679. https://doi.org/10.1007/s11771-022-4947-3

Pu, C., Yang, X., Zhao, H., Chen, Z., Xiao, D., 2021. Numerical investigation on crack propagation and coalescence induced by dual-borehole blasting. Int. J. Impact. Eng. (103983).

Riedel, W., Kawai, N., Kondo, K.I., 2009. Numerical assessment for impact strength measurements in concrete materials. Int. J. Impact. Eng. 36(2), 283-293. https://doi.org/10.1016/j.ijimpeng.2021.103983

Saadatmand Hashemi, A., Katsabanis, P., 2020. The effect of stress wave interaction and delay timing on blast-induced rock damage and fragmentation. Rock. Mech. Rock. Eng. 53(5), 2327-2346. https://doi.org/10.1007/s00603-019-02043-9.

Shen, W.G., Zhao, T., Crosta, G.B., Dai, F., 2017. Analysis of impact-induced rock fragmentation using a discrete element approach. Int. J. Rock. Mech. Min. Sci. 98, 33-38. https://doi.org/10.1016/j.ijrmms.2017.07.014.

Singh, P.K., Roy, M.P., Paswan, R.K., 2014. Controlled blasting for long term stability of pit-walls. Int. J. Rock. Mech. Min. Sci. 70, 388-399. https://doi.org/10.1016/j.ijrmms.2014.05.006.

Song, J.H., Wang, H.W., Belytschko, T., 2008. A comparative study on finite element methods for dynamic fracture. Comput. Mech. https://doi.org/10.1007/s00466-007-0210-x

Tao, J., Yang, X.G., Li, H.T., Zhou, J.W., Lu, G.D., 2020. Numerical investigation of blast-induced rock fragmentation. Comput. Geotech. 128(93), 103846. https://doi.org/10.1016/j.compgeo.2020.103846.

Tose, S.S.J., 2006. A review of the design criteria and practical aspects of developing a successful pre-split. International Symposium on Stability of Rock Slopes in Open Pit Mining and Civil Engineering The South African Institute of Mining and Metallurgy. 525-546.

Wang, H.C., Wang, Z.L., Wang, J.G., Wang, S.M., Wang, H.R., Yin, Y.G., Li, F., 2021a. Effect of confining pressure on damage accumulation of rock under repeated blast loading. Int. J. Impact. Eng. 156(103961). https://doi.org/10.1016/j.ijimpeng.2021.103961.

Wang, J.X., Yin, Y., Esmaieli, K., 2018. Numerical simulations of rock blasting damage based on laboratory-scale experiments. J. Geophys. Eng. 15(6), 2399-2417. https://doi.org/10.1088/1742-2140/aacf17.

Wang, Y.B., Wen, Z.J., Liu, G.Q., Wang, J.G., Bao, Z.Q., Lu, K.Q., Wang, D.C., Wang, B.Z., 2020. Explosion propagation and characteristics of rock damage in decoupled charge blasting based on computed tomography scanning. Int. J. Rock. Mech. Min. Sci. 136(104540). https://doi.org/10.1016/j.ijrmms.2020.104540.

Wang, Z.L., Wang, H.C., Wang, J.G., Tian, N.C., 2021b. Finite element analyses of constitutive models performance in the simulation of blast-induced rock cracks. Comput. Geotech. 135. https://doi.org/10.1016/j.compgeo.2021.104172.

Wei, X.Y., Zhao, Z.Y., Gu, J., 2009. Numerical simulations of rock mass damage induced by underground explosion. Int. J. Rock. Mech. Min. Sci. 46(7), 1206-1213. https://doi.org/10.1016/j.ijrmms.2009.02.007.

Wittel, F., Kun, F., Herrmann, H., Kröplin, B., 2004. Fragmentation of shells. Phys. Rev. Lett. 93(3), 035504. https://doi.org/10.1103/PhysRevLett.93.035504.

Xia, X., Yu, C., Liu, B., Liu, Y., Li, H., 2018. Experimental study on the seismic efficiency of rock blasting and its influencing factors. Rock. Mech .Rock. Eng. 51(8), 2415-2425. https://doi.org/10.1007/s00603-018-1477-2.

Xie, L.X., Lu, W.B., Zhang, Q.B., Jiang, Q.H., Chen, M., Zhao, J., 2017. Analysis of damage mechanisms and optimization of cut blasting design under high in-situ stresses. Tunn. Undergr. Space. Technol. 66, 19-33. https://doi.org/10.1016/j.tust.2017.03.009.

Yan, S.L., Xu, Y., 2005. Numerical simulation of water-coupled charge rock blasting mechanism. Chin. J. Undergr. Space. Eng. 1(6), 921-924.

Yang, R.S., Chen, D.X., Yang, L.Y., Zhen, L., Zheng, C.D., 2019. Study of decoupled charge blasting based on high-speed digital image correlation method. Tunn. Undergr. Space. Technol. 83, 51-59. https://doi.org/10.1016/j.tust.2018.09.031.

Yi, C., Sjöberg, J., Johansson, D., Petropoulos, N., 2017a. A numerical study of the impact of short delays on rock fragmentation. Int. J. Rock. Mech. Min. Sci. 100, 250-254. https://doi.org/10.1016/j.ijrmms.2017.10.026.

Yi, C.P., Johansson, D., Greberg, J., 2017b. Effects of in-situ stresses on the fracturing of rock by blasting. Comput. Geotech. https://doi.org/10.1016/j.compgeo.2017.12.004.

Yu, M.H., 1998. Twin shear theory and its application. Science Press, Beijing.

Yuan, W., Wang, W., Su, X.B., Wen, L., Chang, J.F., 2019. Experimental and numerical study on the effect of water-decoupling charge structure on the attenuation of blasting stress. Int. J. Rock. Mech. Min. Sci. 124(104133). https://doi.org/10.1016/j.ijrmms.2019.104133.

Zhang, A.M., Yang, W.S., Yao, X.L., 2012. Numerical simulation of underwater contact explosion. Appl. Ocean. Res. 34, 10-20. https://doi.org/10.1016/j.apor.2011.07.009.

Zhang, H., Li, T., Wu, S., Zhang, X., Gao, W., Shi, Q., 2022. A study of innovative cut blasting for rock roadway excavation based on numerical simulation and field tests. Tunn. Undergr. Space. Technol. 119(104233). https://doi.org/10.1016/j.tust.2021.104233.

Zhang, S., Wang, G., Chao, W., Pang, B., Du, C., 2014. Numerical simulation of failure modes of concrete gravity dams subjected to underwater explosion. Eng. Fail. Anal. 36(1), 49-64. https://doi.org/10.1016/j.engfailanal.2013.10.001.

Zhu, Z.M., Mohanty, B., Xie, H.P., 2007. Numerical investigation of blasting-induced crack initiation and propagation in rocks. Int. J. Rock. Mech. Min. Sci. 44(3), 412-424. https://doi.org/10.1016/j.ijrmms.2006.09.002.

Zhu, Z.M., Xie, H.P., Mohanty, B., 2008. Numerical investigation of blasting-induced damage in cylindrical rocks. Int. J. Rock. Mech. Min. Sci. 45(2), 111-121. https://doi.org/10.1016/j.ijrmms.2007.04.012.

Zuo, J.J., Yang, R.S., Gong, M., Ma, X.M., Wang, Y.B., 2022. Fracture characteristics of iron ore under uncoupled blast loading. Int. J. Min. Sci. Technol. 32, 657-667. https://doi.org/10.1016/j.ijmst.2022.03.008